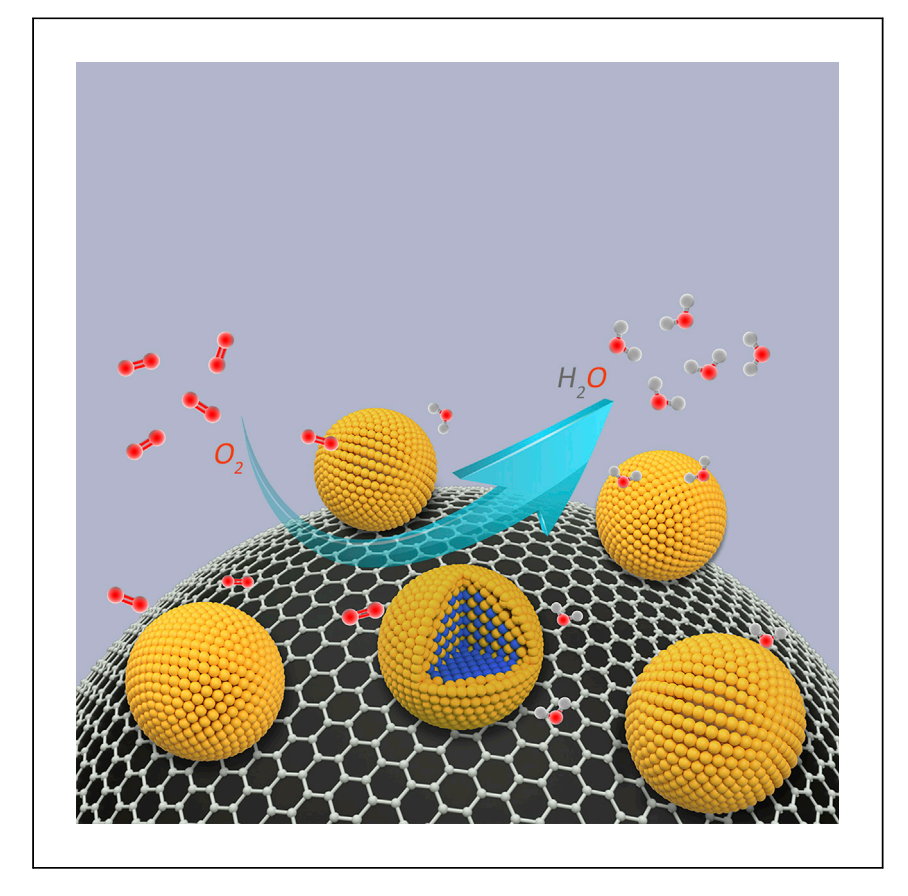
Matter



Article

Amino-tethering synthesis strategy toward highly accessible sub-3-nm L1₀-PtM catalysts for high-power fuel cells



Sub-3-nm PtCo nanoparticles, consisting of an ordered PtCo core and 2–3 atomic layers of Pt shell, exhibit excellent activity and durability for the oxygen reduction reaction. These sub-3-nm PtCo intermetallic nanoparticles, deposited mainly in the opened mesopores of carbon supports, are highly accessible to proton-conducting ionomers and oxygen in the membrane assembly electrode, achieving fuel cell performance that exceeds the DOE targets for light-duty vehicles.

Qing Gong, Hong Zhang, Haoran Yu, ..., David A. Cullen, Ping Liu, Jian Xie

jianxie@iupui.edu

Highlights

Highly accessible sub-3-nm L1₀-PtM particles were synthesized with a high Pt content

Enhanced Pt utilization in the MEA contributed to excellent fuel cell performance

Record-high power density of $0.96~\text{W/cm}^2$ at 0.67~V was achieved in an H_2 /air fuel cell

Meeting nearly all Department of Energy targets for light-duty vehicles



Gong et al., Matter 6, 963–982 March 1, 2023 © 2022 Elsevier Inc. https://doi.org/10.1016/j.matt.2022.12.011



Matter



Article

Amino-tethering synthesis strategy toward highly accessible sub-3-nm L1₀-PtM catalysts for high-power fuel cells

Qing Gong,¹ Hong Zhang,² Haoran Yu,³ Sungho Jeon,⁴ Yang Ren,⁵ Zhenzhen Yang,⁶ Cheng-Jun Sun,⁵ Eric A. Stach,⁴ Alexandre C. Foucher,⁴ Yikang Yu,¹ Matthew Smart,⁷ Gabriel M. Filippelli,⁷ David A. Cullen,³ Ping Liu,^{2,8} and Jian Xie^{1,9,*}

SUMMARY

Because of the poor accessibility of embedded active sites, platinum (Pt)-based electrocatalysts suffer from insufficient Pt utilization and mass transport in membrane electrode assemblies (MEAs), limiting their performance in polymer electrolyte membrane fuel cells. Here, we report a simple and universal approach to depositing sub-3-nm L1₀-PtM nanoparticles over external surfaces of carbon supports through pore-tailored amino (NH₂)-modification, which enables not only excellent activity for the oxygen reduction reaction, but also enhanced Pt utilization and mass transport in MEAs. Using a low loading of 0.10 mg_{Pt}·cm⁻², the MEA of PtCo/KB-NH₂ delivered an excellent mass activity of 0.691 A·mg_{Pt}⁻¹, a record-high power density of 0.96 W·cm⁻² at 0.67 V, and only a 30-mV drop at 0.80 A cm⁻² after 30,000 voltage cycles, which meets nearly all targets set by the Department of Energy. This work provides an efficient strategy for designing advanced Pt-based electrocatalysts and realizing high-power fuel cells.

INTRODUCTION

Polymer electrolyte membrane (PEM) fuel cells are promising energy conversion devices for automotive and stationary applications because of their zero-carbon emissions and high efficiency. Platinum nanoparticles supported over carbon surfaces (Pt/C) are commercially used to catalyze the sluggish oxygen reduction reaction (ORR) on the cathode side of membrane electrode assemblies (MEAs). Unfortunately, the high cost, low ORR activity, and unsatisfactory durability of Pt/C catalysts strictly hinder large-scale adoption of PEM fuel cells. 1-3 An effective strategy to reduce Pt usage while enhancing activity is to form Pt-based alloys with transition metals (M) such as Fe, Co, Ni, Zn, etc. 1,4-6 In particular, Pt-Co and Pt-Ni alloys are two of the most active Pt-based catalysts. The activity enhancement can be ascribed to the favorable ligand and strain effects on the surface of Pt, which are known to weaken the adsorption of oxygenated intermediates in the related rate-determining steps. 7-11 Because Pt and M atoms in Pt-M alloys are randomly distributed in a facecentered cubic (fcc) lattice, the M atoms can be rapidly leached out when subjected to the corrosive environment of PEM fuel cells, resulting in degradation of catalytic kinetics and poisoning of electrodes and membranes. 12-14

Ordered Pt-based intermetallics are considered promising candidates to achieve excellent activity and high durability in fuel cell applications.^{2,15–17} Face-centered

PROGRESS AND POTENTIAL

Polymer electrolyte membrane (PEM) fuel cells are attractive energy conversion devices for electric vehicles, particularly medium- and heavy-duty vehicles. However, current platinum (Pt)based catalysts for the cathode oxygen reduction reaction suffer from insufficient activity and durability in membrane electrode assemblies (MEAs), limiting the practical application of PEM fuel cells. Here, we report a synergistic strategy to prepare highly active and stable sub-3-nm Pt-based intermetallic catalysts while overcoming the low Pt utilization and insufficient mass transport issues in the MEA, enabling breakthrough fuel cell performance. The core-shellstructured L1₀-PtCo@Pt nanoparticles meet nearly all performance requirements for light-duty vehicles set by the Department of Energy and demonstrate great potential for application in heavy-duty vehicles. This synergistic strategy provides a novel and effective avenue for designing advanced catalysts for fuel cell applications.







tetragonal (fct) L1₀-PtM and cubic L1₂-Pt₃M are two typical ordered Pt-based alloys in which Pt and M atoms occupy specific lattice sites and have fixed atomic ratios. Compared with the L1₂-Pt₃M structure, L1₀-PtM is beneficial for further reducing the Pt content but has been less studied. The L1₀-PtM intermetallic structure provides a strong electronic interaction between M (3d) and Pt (5d) atomic orbitals along the crystallographic c direction, which could protect M atoms from oxidation and, thus, leaching. 18-20 Generally, L1₀-PtM structures are formed by high-temperature (≥600°C) heat treatment of disordered PtM counterparts because atomic ordering is a thermally driven process. 16,21 However, under traditional processing conditions, high temperature would inevitably leads to migration and agglomeration of PtM nanoparticles, forming undesirably large and non-uniform particles, resulting in a low electrochemical surface area (ECSA) and, thus, unsatisfactory catalytic performance.²² The preferred size of Pt-based nanoparticles for ORR catalysis is considered to be 2-3 nm with a narrow size distribution. 4,23,24 To overcome particle agglomeration, a typical strategy is to individually prepare PtM nanoparticles using organic surfactants, deposit them on carbon supports, followed by high-temperature heat treatment. $^{18-20,25-32}$ Unsatisfactory particle size (≥ 5 nm), low Pt loading (\leq 10 wt %), and weak catalyst-carbon interaction are common drawbacks for this synthesis strategy. Low Pt loadings on carbon supports may increase mass transport resistance in MEAs because of thicker catalyst layers, whereas weak catalyst-carbon interaction is detrimental to catalyst durability. Another synthesis strategy is to utilize protective coatings such as SiO₂, ³³ MgO, ^{18,20,25} and carbonized polymers^{34–38} to hinder migration and aggregation of PtM nanoparticles during high-temperature heat treatment. Although this method can reduce the particle size to 3-6 nm, it is difficult to completely remove the protective coatings, leaving surface residues to block the active sites and, thus, increase mass transport resistance. Therefore, it is of paramount importance to develop a simple method to directly deposit ultrafine (<3 nm) and uniform L1₀-PtM intermetallic nanoparticles with a reasonable Pt loading (>20 wt %) on carbon supports.

Numerous Pt-based catalysts have shown encouraging intrinsic activity in liquid halfcell testing using the rotating disk electrode (RDE) technique. However, translating these outstanding intrinsic activities into fuel cell performance is a considerable challenge.^{3,39} The RDE technique maximizes catalyst utilization and minimizes mass transport resistance by simplifying the reaction zone from a three-phase interface to a two-phase interface, to which the dissolved oxygen and protons in liquid electrolytes are supplied through the electrode rotation. To enhance the active-site density for liquid half-cell testing, highly active Pt-based nanoparticles are almost exclusively supported on high surface-area carbon, in which large amounts of nanoparticles are embedded in micropores of carbon support. However, when such a catalyst is incorporated into a catalyst layer of MEAs, the embedded active sites are poorly accessible to reactants of oxygen and protons, leading to ineffective utilization of the inside active sites and additional mass transport resistance. ^{39,40} This results in unsatisfactory MEA performance at practical working voltages. For instance, in H₂/air fuel cells using a cathode loading below 0.125 mg_{Pt}·cm⁻², the maximum rated power density (at 0.67 V) reported in published literature is around 0.82 W·cm⁻² (Table S1), which is well below the Department of Energy (DOE) target of 1.0 W·cm⁻² for transportation applications. Pore engineering of carbon supports is an effective approach to improve catalyst utilization and mass transport in the catalyst layers. Pt nanoparticles mainly located in opened mesopores of carbon supports, appearing primarily on the carbon external surface, are known to be easily accessible to reactants, 41,42 which are desired for high-performance MEAs.

¹Department of Mechanical and Energy Engineering, Purdue School of Engineering and Technology, Indiana University-Purdue University Indianapolis, Indianapolis, IN 46202, USA

²Department of Chemistry, Stony Brook University, Stony Brook, NY 11794, USA

³Center for Nanophase Materials Sciences, Oak Ridge National Laboratory, Oak Ridge, TN 37831,

⁴Department of Materials Science and Engineering, University of Pennsylvania, Philadelphia, PA 19104, USA

⁵X-Ray Science Division, Argonne National Laboratory, Lemont, IL 60439, USA

⁶Chemical Sciences and Engineering Division, Argonne National Laboratory, Lemont, IL 60439, **USA**

⁷Department of Earth Sciences, Purdue School of Science, Indiana University-Purdue University Indianapolis, Indianapolis, IN 46202, USA

⁸Chemistry Division, Brookhaven National Laboratory, Upton, NY 11973, USA

*Correspondence: jianxie@iupui.edu https://doi.org/10.1016/j.matt.2022.12.011





It is thus clear that ultrafine L1₀-PtM nanoparticles uniformly distributed on carbon supports with reasonable Pt loading and high accessibility are desirable for fuel cell applications. Here we report a simple and universal strategy to directly synthesize highly accessible sub-3-nm L1₀-PtM intermetallic nanoparticles on carbon supports. Synthesis of such L1₀-PtM intermetallic nanoparticles relied on monodisperse Pt nanoparticles supported on NH2-modified carbon as seeds, which is achieved through a strong electrostatic attraction established between the Pt-precursor (PtCl₆²⁻) and protonated ammonium ions (NH₃⁺) immobilized over carbon surfaces. The NH₂ modification tailored the pore structure of carbon supports, enabling deposition of L1₀-PtM intermetallic nanoparticles mainly in the opened mesopores of carbon surfaces, which are highly accessible to reactants of oxygen and protons in MEAs. In this work, we focused on preparation of sub-3-nm L1₀-PtCo nanoparticles supported on NH2-modified Ketjenblack (PtCo/KB-NH2). PtCo/KB-NH2 exhibited excellent ORR activity and durability, originating from the favorable structure of 2-3 atomic Pt layers formed over the L1₀-PtCo core. Benefitting from the high accessibility of PtCo/KB-NH2 nanoparticles, the MEA delivered enhanced Pt utilization and lowered mass transport resistance, resulting in breakthrough fuel cell performance.

RESULTS AND DISCUSSION

The synthesis scheme of L1₀-PtCo nanoparticles supported on NH₂-modified carbon is illustrated in Figure 1A. The NH₂-modified carbon was initially synthesized utilizing a diazonium reaction based on our previous study. 43,44 The N 1s spectra of X-ray photoelectron spectroscopy (XPS) in Figure 1B demonstrated successful covalent grafting of p-benzene amino (-NH₂) groups over the surface of Ketjenblack (KB) carbon with a surface N content of 4.4 atom %. The -NH₂ groups significantly blocked the small pores of KB, which led to a remarkable decrease in Brunauer-Emmett-Teller (BET)-specific surface area from 769 m²·g⁻¹ of KB to 170 m²·g⁻¹ of KB-NH₂ (Figure 1C). Apparently, KB contains large numbers of micropores (<2 nm) with a high specific micropore volume of 0.20 $\text{cm}^3 \cdot \text{g}^{-1}$, which was decreased by 90.0% after modification for KB-NH₂ (0.02 cm³·g⁻¹). However, the specific volume of mesopores (2-50 nm) remained at a high level of 0.72 cm³·g⁻¹ for KB-NH₂, implying a slight reduction of 8.0% relative to that of KB (Figure S1A). Catalyst nanoparticles embedded in the micropores of carbon supports are poorly accessible to proton-conducting ionomers and oxygen in the MEA, whereas sufficient mesopores could ensure efficient access of protons/ oxygen and facilitate formation of desired catalyst/ionomer interfaces. 39,40 For the subsequent Pt deposition, a modified ethylene glycol (EG) method was employed. The Pt complex ions (PtCl₆²⁻) in the EG aqueous solution and protonated ammonium ions (NH3+) on the KB-NH2 surface exhibited opposite charges, resulting in a strong electrostatic attraction.⁴⁴ Apparently, this attraction guided the Pt complex ions to land uniformly on the carbon surface, enabling deposition of fine monodisperse Pt nanoparticles on the KB-NH₂ (Figure 1E). For Pt/KB-NH₂ with a Pt content of 8.0 wt %, the average size of Pt nanoparticles was determined to be 1.5 \pm 0.3 nm. As a comparison, the Pt nanoparticles deposited on the KB exhibited a larger average size and a wider size distribution of 1.6 \pm 0.5 nm (Figure S2) because of the lack of electrostatic attraction guidance. Homogeneous grafting of -NH2 onto KB-NH2 was demonstrated by the uniform deposition of Pt nanoparticles on KB-NH₂. A strong electronic interaction between Pt nanoparticles and KB-NH₂ was revealed in the Pt/KB-NH₂ spectra, as evidenced by considerably positive shifts in the XPS binding energies of N 1s and Pt 4f spectra relative to those of KB-NH₂ (Figure 1B) and Pt/KB (Figure S1D), respectively. 43 Such an



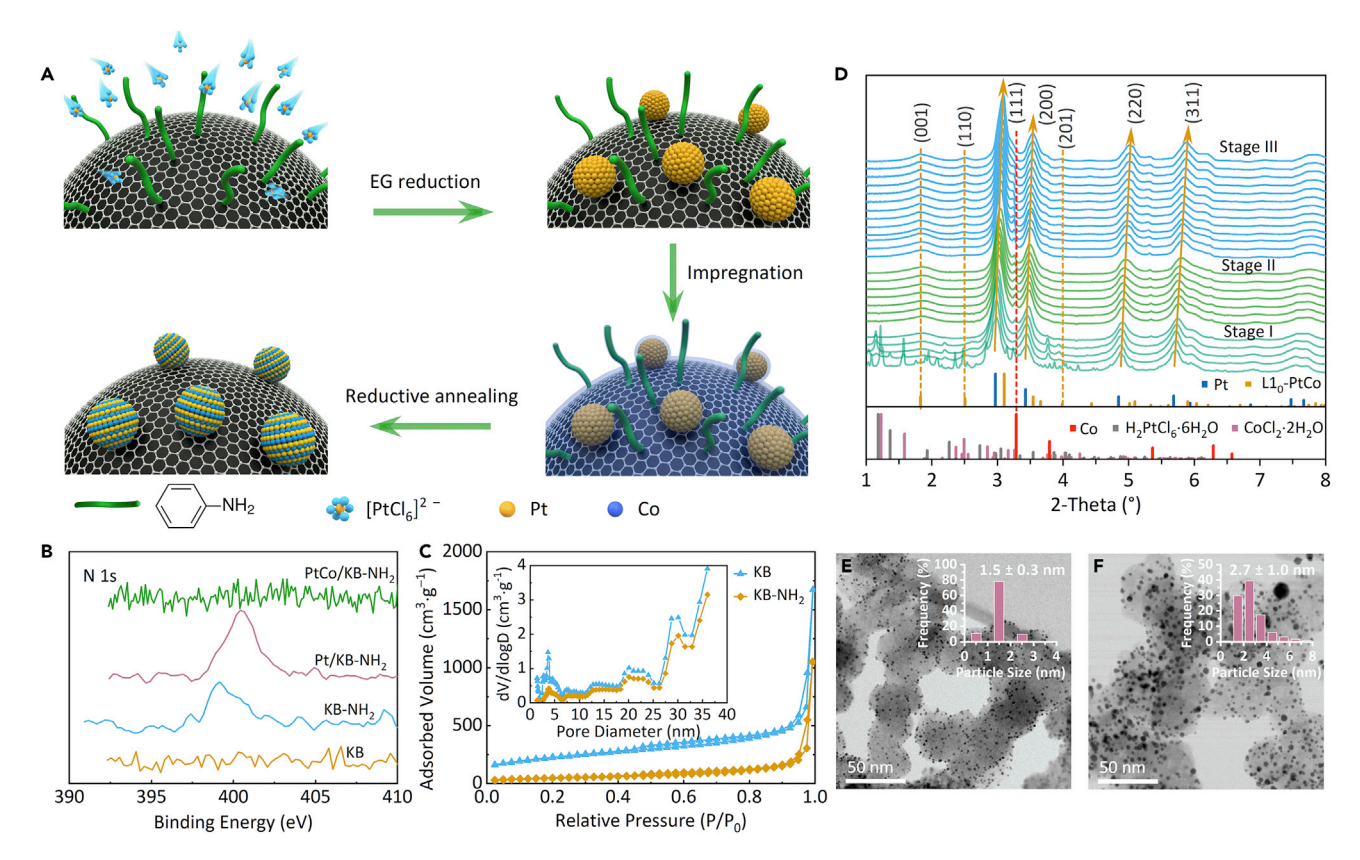


Figure 1. Structure evolution and formation of PtCo/KB-NH2 nanoparticles

- (A) Synthesis schematic of $PtCo/KB-NH_2$ nanoparticles.
- (B) XPS N 1s spectra of KB, KB-NH $_2$, Pt/KB-NH $_2$, and PtCo/KB-NH $_2$.
- (C) Nitrogen adsorption/desorption isotherms and DFT pore size distributions (inset) of KB and KB-NH $_2$.
- (D) In situ SHEXRD patterns for the structure evolution of PtCo/KB-NH₂ during the heat treatment. The standard lines of Co (PDF#15-0806), Pt (PDF#04-0802), L1₀-PtCo (PDF#65-8969), CoCl₂·2H₂O (PDF#73-0311), and H₂PtCl₆·6H₂O (PDF#85-0162) are included for comparison.
- (E and F) TEM images and corresponding particle size distributions (inset) of (E) $Pt/KB-NH_2$ and (F) $PtCo/KB-NH_2$. Scale bars: 50 nm.

electronic interaction would provide an anchoring effect for Pt nanoparticles and retard particle migration and coalescence during the subsequent annealing process.

To obtain L1₀-PtCo nanoparticles supported on KB-NH₂, Pt/KB-NH₂ was impregnated with Pt and Co precursors, followed by heat treatment under a forming gas atmosphere. The uniform and fine Pt nanoparticles on KB-NH₂ served as seeds to guide deposition of Pt and Co precursors and the subsequent formation/growth of PtCo alloy nanoparticles. As shown in Figure 1D, the structure evolution and formation of L1₀-PtCo intermetallic nanoparticles during the heat treatment were investigated using in situ synchrotron high-energy X-ray diffraction (SHEXRD), which could be divided into three stages based on the annealing process. The first stage was a heating process from room temperature to 400°C, which clearly revealed reduction of the Co precursor (CoCl₂·2H₂O) and Pt precursor (H₂PtCl₆·6H₂O), accompanied by slight alloying (positive shifting of (111), (200), (220), and (311) peaks). The second stage was a 2-h hold at 400°C, which corresponded to further alloying as the Co atoms continuously diffused into the Pt fcc lattice. For the third stage, the heat treatment temperature was increased to 650°C, during which the characteristic peaks of the L10-PtCo structure gradually appeared, accompanied by further alloying. The intensity of peaks indexed to the (001), (110), and (201)





planes for the L10-PtCo structure gradually increased with heating time, which is attributed to the gradual structure transformation from a disordered PtCo alloy to an atomically ordered L1₀-PtCo intermetallic. Although the presence of -NH₂ groups may improve the uniformity of ionomer distribution in the catalyst layers, their stability has been demonstrated to be insufficient to withstand harsh fuel cell testing conditions, resulting in decreased durability. 42,45 The -NH₂ groups on the carbon surface were decomposed during the high-temperature heat treatment (Figure S1B), as evidenced by disappearance of the XPS N 1s peak in PtCo/KB-NH₂ (Figure 1B), which may be beneficial to maintain the durability of L1₀-PtCo nanoparticles. To ensure formation of the L1₀-PtCo structure, a slight excess of Co precursor was introduced during the impregnation step. After heat treatment at 650°C for 6 h, a post-acid treatment was performed to remove the excessive metallic Co on the carbon surface. Based on inductively coupled plasma atomic emission spectroscopy (ICP-AES) analyses, the Pt loading of the resulting PtCo/KB-NH2 was determined to be 24.0 wt %. As shown in Figure 1F, the PtCo nanoparticles for PtCo/KB-NH₂ were uniformly distributed over the carbon surface with an average size of 2.7 \pm 1.0 nm. As a comparison, the PtCo nanoparticles for PtCo/KB (Pt loading of 23.5 wt %), prepared using a similar procedure except for carbon modification, showed a larger average size and a wider size distribution of 3.0 \pm 1.5 nm (Figures S4 and S5). PtCo/KB-NH₂ and PtCo/KB exhibited more uniform and much smaller nanoparticles compared with the PtCo/KB-traditional (6.2 \pm 2.5 nm, Pt loading of 24.6 wt %), prepared using a traditional impregnation method without carbon modification or seed mediation (Figure S6). Clearly, seed mediation enabled effective deposition of fine intermetallic nanoparticles over the carbon surface, and NH₂ modification further improved the uniformity of Pt nanoparticle seeds, resulting in more uniform and fine L1₀-PtCo nanoparticles of PtCo/KB-NH₂. An L1₀ intermetallic PtFe/KB-NH₂ catalyst with an average particle size of 2.6 \pm 0.9 nm (Figure S7) and L1₀ intermetallic PtCo/VC-NH₂ catalyst with an average particle size of 3.4 \pm 1.1 nm (Figure S8) were also obtained using our synthesis strategy, which demonstrates that this approach can be used for different PtM intermetallic catalysts and carbon supports. For the sake of simplification, we focus on the structure and performance analysis of PtCo/ KB-NH₂ in the remainder of this report.

The location of Pt nanoparticles relative to the internal or external surface of carbon supports is known to affect the MEA performance of Pt/C catalysts. 41,42 The Pt nanoparticles on the external surface of carbon supports are readily accessible to reactants of oxygen and protons, which is beneficial for maximizing the catalyst/ionomer interface and lowering the mass transport resistance in the catalyst layer. To understand the distribution of PtCo nanoparticles on the internal and external surfaces, scanning transmission electron microscopy (STEM) was used to simultaneously acquire secondary electron (SE) and high-angle annular dark-field (HAADF) images, as shown in Figures 2A-2D. The SE images reveal PtCo nanoparticles only on the top surface of carbon supports, whereas PtCo nanoparticles on the external and internal surfaces are visible in the HADDF image. 41,42 The percentage of PtCo nanoparticles on the external surface for PtCo/KB-NH₂ (Figures 2C and 2D) is much higher than that for PtCo/KB (Figures 2A and 2B), which may be due to the fact that most PtCo nanoparticles for PtCo/KB-NH2 are deposited in the opened mesopores, whereas a large number of PtCo nanoparticles for PtCo/KB reside in the internal micropores. The sufficient mesopores of KB-NH₂ enabled formation of L1₀-PtCo nanoparticles to be primarily deposited on the external surface. It is estimated that 93% and 41% of PtCo nanoparticles are located on the external surface for PtCo/KB-NH₂ and PtCo/KB, respectively, which agrees well with the observations on Pt seed counterparts (Figure S3) and commercial Pt/KB reported previously, 41



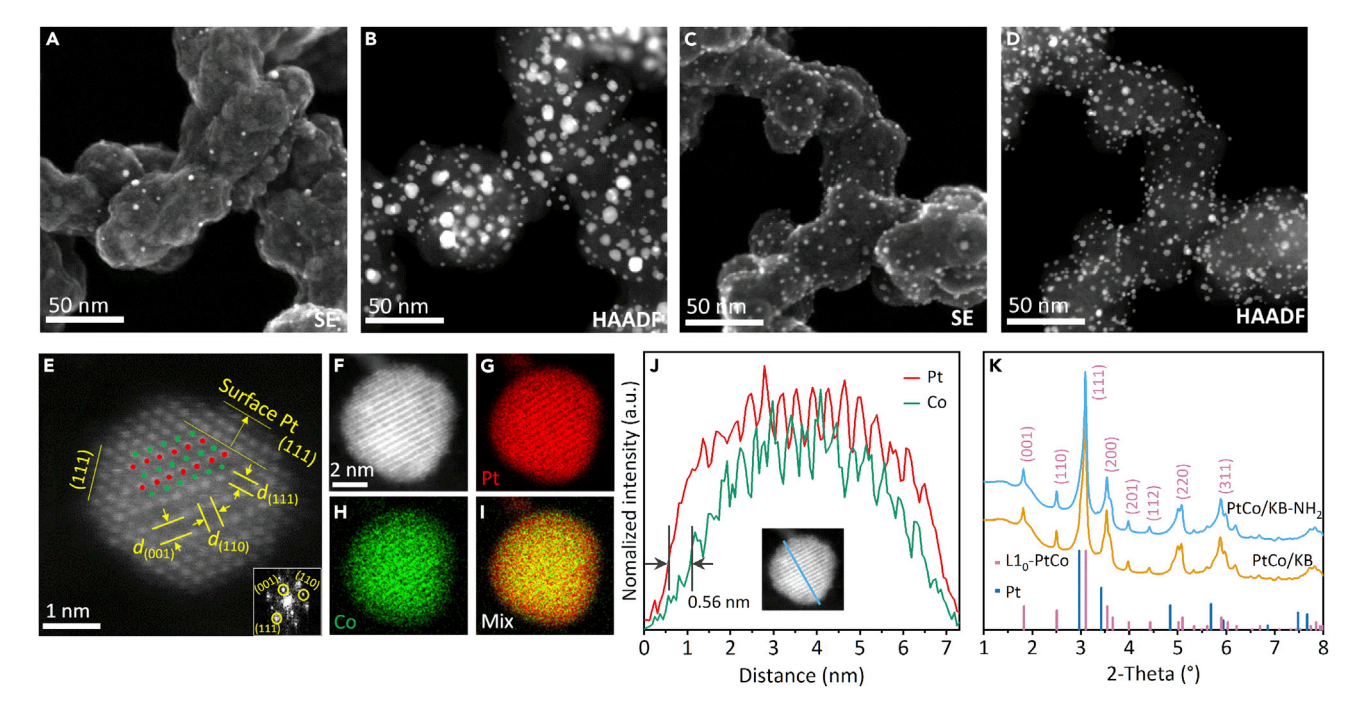


Figure 2. Distribution information and structure characterization of PtCo/KB and PtCo/KB-NH₂ nanoparticles
(A–D) STEM images of (A and B) PtCo/KB and (C and D) PtCo/KB-NH₂ ([A] and [C] are SE images, [B] and [D] are HAADF images).
(E–J) Atomic-resolution STEM image and corresponding FFT pattern ([E], inset), EDS elemental maps (F–I), and line-scan profiles (J) of L1₀-PtCo nanoparticles in PtCo/KB-NH₂.

(K) SHEXRD patterns of PtCo/KB and PtCo/KB-NH $_2$ catalysts. Scale bars: 50 nm (A–D), 1 nm (E), and 2 nm (F).

confirming effective control of seed guidance over precursor deposition and subsequent formation of L1₀-PtCo nanoparticles. Atomic-resolution STEM was employed to investigate the detailed structure of PtCo/KB-NH2 nanoparticles. A representative PtCo nanoparticle is illustrated in Figure 2E, showing 2-3 atomic Pt layers over an L1₀-PtCo core. The atomically ordered structure of the L1₀-PtCo core was evidenced by the alternating arrangement of high (Pt) and low (Co) Z-contrast along the [110] direction. Two lattice fringes with d-spacing values of 0.370 and 0.269 nm were observed in the core, corresponding to the (001) and (110) planes of the L1₀-PtCo structure, respectively. The superlattice spots indexed to the (001) and (110) planes in the inset fast Fourier transform (FFT) pattern also confirmed formation of the L1₀-PtCo structure. The L1₀-PtCo core was found to be bounded by (111) facets covered with Pt, which is known to be highly active for ORR catalysis. 46-48 STEM-energy-dispersive X-ray spectrum (EDS) elemental maps of a single particle, shown in Figures 2F-2I, confirmed that the alternating contrast in the core arises from ordered rows of Pt and Co in the particle core, consistent with the ordered L10-PtCo structure, along with the presence of a Pt-rich surface layer. According to the line scan profile (Figure 2J), the shell thickness was estimated to be 0.56 nm, which is about 2-3 atomic Pt layers. The atomic ratio of Pt/Co for PtCo/KB-NH₂ was determined to be 72/28, which is a reasonable value considering that the ultrafine L1₀-PtCo nanoparticles were subjected to post-acid treatment. The SHEXRD patterns of PtCo/KB-NH₂ and PtCo/KB in Figure 2K matched well with the L1₀-PtCo structure. The diffraction peaks corresponding to the (111), (200), (220), and (311) planes are shifted to larger Bragg angles compared with the standard lines for pure Pt, indicating that smaller Co atoms were incorporated into the Pt fcc lattice and caused



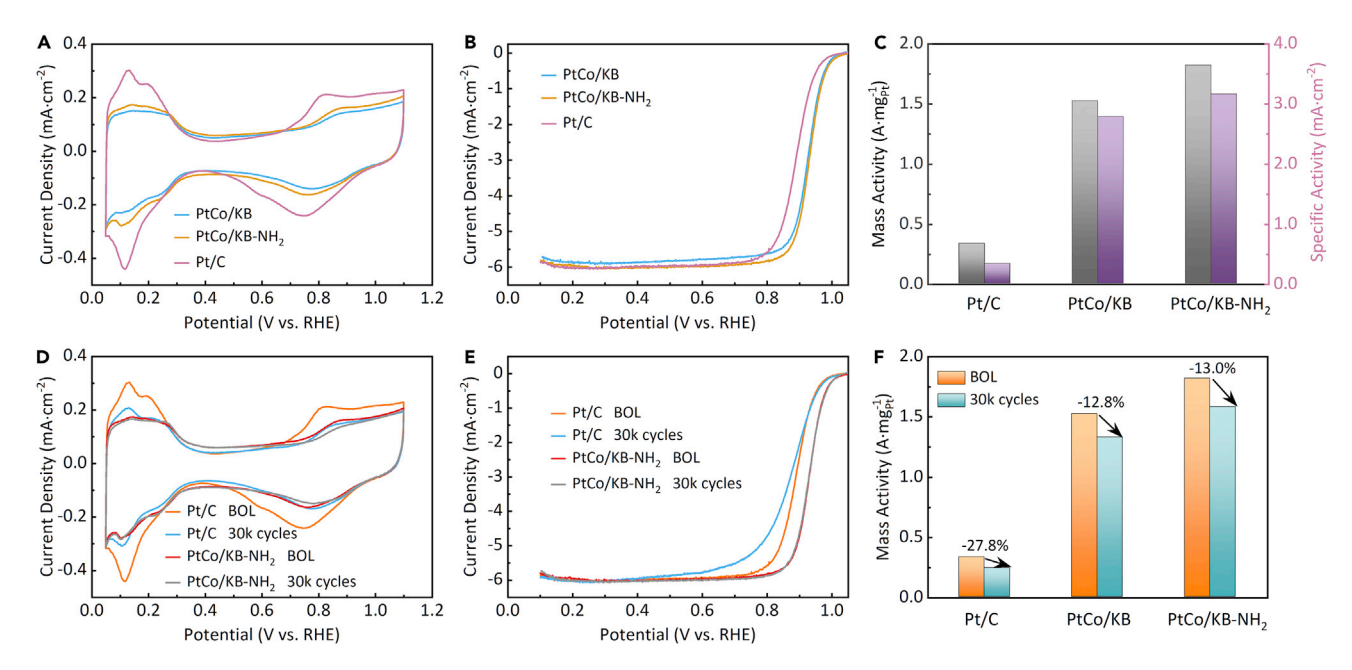


Figure 3. Electrocatalytic performance of commercial Pt/C, PtCo/KB, and PtCo/KB-NH₂ catalysts tested using the RDE technique (A and B) CV curves (A) and ORR polarization curves (B) for $0.1 \text{ mol} \cdot \text{L}^{-1} \text{ HClO}_4$ solution.

(C) MA and SA obtained at 0.9 V_{iR-free}.

(D and E) CV curves (D) and ORR polarization curves (E) tested at the beginning of life (BOL) and after 30,000 potential cycles between 0.60 and 0.95 V in 0.1 mol·L $^{-1}$ HClO₄ solution.

(F) Variations of MA after 30,000 potential cycles.

lattice contraction. Four well-defined peaks indexed to the (001), (110), (201), and (112) planes of the L1₀-PtCo structure are considered to be indicators of ordered structure formation. The relative value of the measured intensity ratio of I_{110}/I_{111} to the theoretical one can be used to evaluate the degree of ordering for the L1₀ intermetallic structure. ^{26,32,49} The degree of ordering was estimated to be 52% and 55% for PtCo/KB-NH₂ and PtCo/KB, respectively, which are reasonable values considering the presence of disordered Pt shells over the ultrafine L1₀-PtCo core.

The ORR performance of PtCo/KB-NH2 and PtCo/KB catalysts was investigated using the RDE technique in 0.1 mol·L⁻¹ HClO₄ electrolytes. For comparison, one of the most active commercial Pt/C catalysts (TEC10E50E, Tanaka Kikinzoku Kogyo) was also tested under the same conditions. As shown by cyclic voltammetry (CV) curves (Figure 3A), both PtCo catalysts exhibited apparent shrinkages in the hydrogen absorption/desorption (HAD) regions compared with commercial Pt/C, implying that part of the Pt atoms cannot be used for HAD because of incorporation of Co atoms. The potentials associated with surface oxidation and oxide reduction were positively shifted for both PtCo catalysts relative to commercial Pt/C, suggesting weakened oxophilicity of surface Pt. The ECSA determined from corresponding HAD regions was 54.3, 57.6, and 98.9 $\text{m}^2 \cdot \text{g}_{\text{Pt}}^{-1}$ for PtCo/KB, PtCo/KB-NH₂, and commercial Pt/C, respectively. Because of the smaller particle size, PtCo/KB-NH₂ had a larger ECSA than PtCo/KB, which is about 2.1 times larger than L10-PtCo/C with an average particle size of 8.9 nm reported previously. ¹⁹ Using the CO stripping method, the ECSA of commercial Pt/C was determined to be 101.0 m $^2 \cdot g_{Pt}^{-1}$, close to the value obtained from the HAD method (98.9 $\text{m}^2 \cdot \text{g}_{\text{Pt}}^{-1}$). The enhanced ECSA could be obtained using the CO stripping method (Figure S9) for PtCo/KB-NH₂ (73.5 $\text{m}^2 \cdot \text{g}_{\text{Pt}}^{-1}$) and PtCo/KB (71.1 $\text{m}^2 \cdot \text{g}_{\text{Pt}}^{-1}$), indicating formation of a Pt-rich shell over the alloy structure. ⁵⁰ Because the CO stripping method may alter the structure





and composition of Pt-based alloy particles, 51,52 the ECSA values determined from the HAD method were used for the calculations below. For ORR polarization curves (Figure 3B), PtCo/KB-NH₂ delivered a half-wave potential ($E_{1/2}$) of 0.93 V, which is higher than PtCo/KB (0.92 V) and commercial Pt/C (0.89 V), implying enhanced ORR activity. Mass activity (MA) and specific activity (SA) were calculated by normalizing the kinetic current at 0.90 V over Pt loading and ECSA, respectively. As shown in Figure 3C, PtCo/KB-NH₂ showed excellent MA (1.82 A·mg_{Pt}⁻¹) and SA (3.16 mA·cm $^{-2}$), revealing 5.5- and 9.3-time enhancements over commercial Pt/C (MA, 0.33 A·mg_{Pt}⁻¹; SA, 0.34 mA ·cm⁻²), representing one of the most active Ptbased electrocatalysts. PtCo/KB had lower MA (1.53 $A \cdot mg_{Pt}^{-1}$) and SA (2.78 mA·cm⁻²), but it was still much higher than commercial Pt/C. Catalyst durability was examined by performing 30,000 potential cycles between 0.60 and 0.95 V at room temperature. PtCo/KB-NH₂ (Figures 3D and 3E) and PtCo/KB (Figure \$10) showed excellent durability with minor changes in ORR polarization and CV curves. In contrast, the $E_{1/2}$ of commercial Pt/C decreased by 17 mV, and ECSA dropped by 27.5%. As shown in Figure 3F, the MA of commercial Pt/C decreased by 27.8%, whereas that of PtCo/KB and PtCo/KB-NH₂ dropped by only 12.8% and 13.0%, respectively, after 30,000 cycles. The MA of PtCo/KB-NH₂ maintained a high level of 1.58 A·mg_{Pt}⁻¹ after 30,000 cycles, approaching 6.6 times that of commercial Pt/C (0.24 A·mg_{Pt}⁻¹).

To understand the excellent activity and durability of PtCo/KB-NH₂, XPS and X-ray absorption spectroscopy (XAS) were employed to characterize these catalysts. As illustrated by the XPS results (Figure 4A), PtCo/KB-NH₂ exhibited a positive shift in the binding energy of the Pt 4f spectrum relative to that of commercial Pt/C, implying a strong electronic interaction between Pt and Co atoms. This electron effect may cause a downward shift in the d-band center of surface Pt, which is known to be favorable for enhancing ORR kinetics.^{8,11} The metallic Pt⁰ content of surface Pt in PtCo/KB-NH₂ (80.6%) was much higher than that in commercial Pt/C (50.6%), consistent with observations on other Pt-based intermetallic catalysts, 53-55 indicating enhanced resistance against Pt oxidation in PtCo/KB-NH2. The enhanced resistance against Pt oxidation agreed well with the observations from the CV curves (Figure 3A) and the Pt L₃-edge extended X-ray absorption fine structure (EXAFS) spectra (Figure 4B), which would apparently improve catalyst durability. In the Pt L₃-edge EXAFS spectrum, the distinct peak around 1.64 Å associated with the Pt-O coordination in commercial Pt/C was not observed in Pt foil and PtCo/KB-NH₂.⁵⁴ As shown in Table S2, the fitted length of the Pt-Pt bond in PtCo/KB-NH₂ (2.70 Å) was much shorter than that in Pt foil (2.76 Å), indicating that smaller Co atoms entered the Pt lattice and formed the PtCo alloy. Shortening of the Pt-Pt bond would inevitably induce a compressive strain over surface Pt, which is known to weaken the adsorption of oxygenated intermediates and therefore accelerate ORR kinetics. 10,11

To gain deep insight into the ORR reactivity of PtCo/KB-NH₂, density functional theory (DFT) calculations were performed to simulate a 2.6-nm-sized L1₀-PtCo@ Pt_{3L} (3 atomic Pt layers over a L1₀-PtCo core) nanoparticle using a semispherical model (right insets in Figure 4C). The results revealed a compressive strain of 3.42% in the Pt-Pt bond on the (111) facet with respect to the fcc Pt bulk. It is known that relatively strong adsorption to oxygenated intermediates (O*, OH*, etc.) limits the ORR kinetics of pure Pt.^{7,11,56} The binding energy of OH* (E_{OH*}) on a metal surface was recently identified as a key descriptor for ORR kinetics, and optimum ORR activity was expected to be achieved at an E_{OH*} of roughly \sim 0.12–0.14 eV weaker than that of unstrained Pt (111).^{7,11} To reduce the computational cost, the E_{OH*} was calculated using a slab model (top insets in Figure 4C),



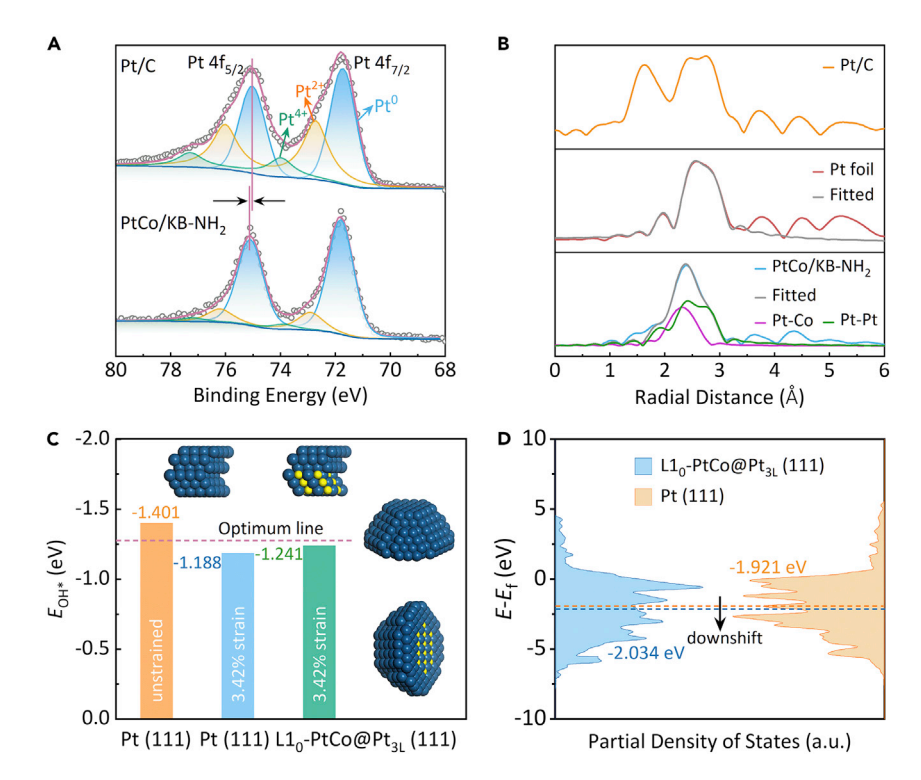


Figure 4. Characterization analyses and DFT calculations for Pt/C and PtCo/KB-NH₂ catalysts (A) XPS Pt 4f spectra for commercial Pt/C and PtCo/KB-NH₂.

- (B) Pt L₃-edge EXAFS spectra for commercial Pt/C, Pt foil, and PtCo/KB-NH₂.
- (C) Calculated E_{OH^*} on L1₀-PtCo@Pt_{3L} (111) with 3.42% compressive strain, Pt (111) with 3.42% compressive strain, and unstrained Pt (111). The top insets show slab models, and the right insets show semispherical models for a 2.6-nm L1₀-PtCo@Pt_{3L} nanoparticle, where blue and yellow spheres represent Pt and Co atoms, respectively.
- (D) Partial density of states (PDOS) of Pt 5d states on unstrained Pt (111) and L1₀-PtCo@Pt_{3L} (111) with 3.42% compressive strain.

and then the strain obtained using the semispherical model (right insets in Figure 4C) was imposed to account for the nanoscale effects on the structure, which was found to be essential to calculate the ORR activity.⁵⁷ As shown in Figure 4C, the $E_{\rm OH^{\star}}$ on L1₀-PtCo@Pt_{3L} (111) with a compressive strain of 3.42% was calculated to be -1.241 eV, which is 0.16 eV weaker than that on unstrained Pt (111) and much closer to the optimum $E_{\text{OH}^{\star}}$. This weakened $E_{\text{OH}^{\star}}$ is associated with a 0.113-eV downshift of the d-band center on L1₀-PtCo@Pt_{3L} (111) relative to Pt (111) based on the calculated partial density of states (PDOS) (Figure 4D), which led to the enhanced ORR kinetics. To separate the influence of ligand effect and strain effect on E_{OH^*} , the same 3.42% compressive strain was applied to the Pt (111) surface. The E_{OH^*} varied dramatically from -1.401 eV on unstrained Pt (111) to -1.188 eV on 3.42% strained Pt (111), going from too strong to too weak compared with the theoretical optimum value, which indicates that the strain-induced variation reached as high as 0.213 eV. The strain is positively correlated with E_{OH^*} on Pt (111) and L1₀-PtCo@Pt_{3L} (111); that is, the increased strain resulted in higher E_{OH^*} (Figure S11B). Because of the presence of Co atoms deep in the core structure, the influence of the ligand effect on $E_{\mathrm{OH}^{\star}}$ is subtle but not negligible compared with the strain effect. The E_{OH*} on L1₀-PtCo@Pt_{3L} (111) is 0.053 eV lower than that on Pt (111) when the same 3.42% compressive strain is applied, implying that the presence of the L1₀-PtCo core (ligand effect)





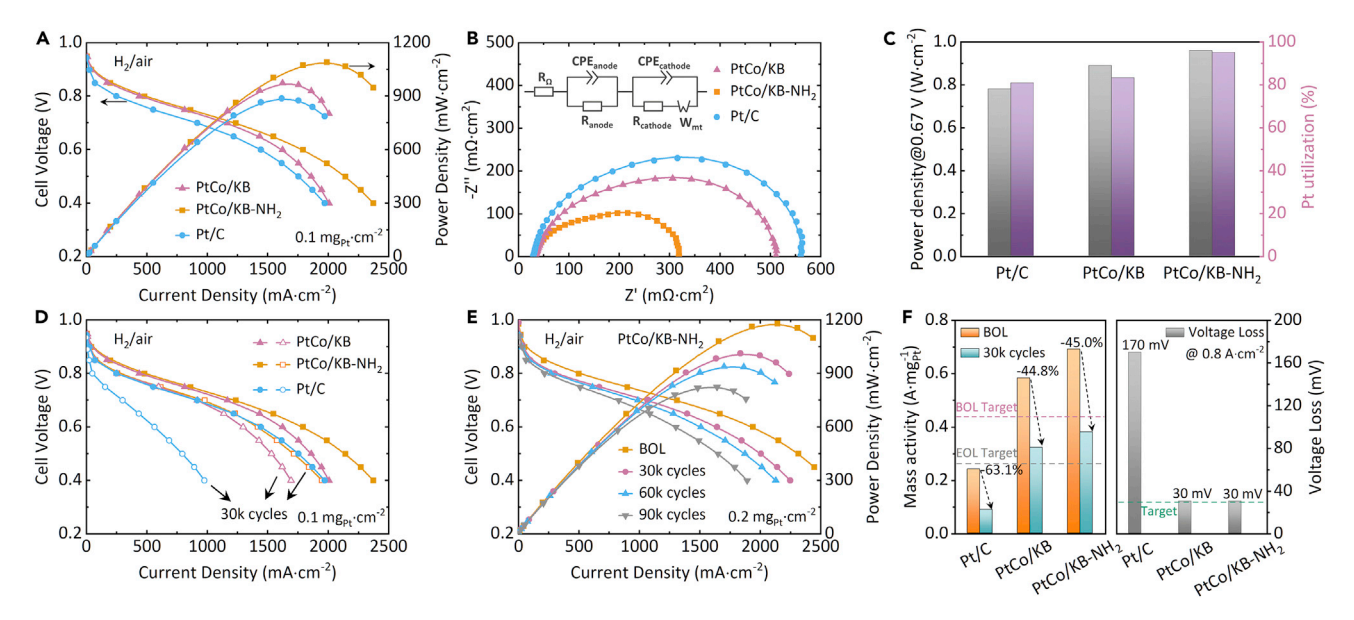


Figure 5. Fuel cell testing results of commercial Pt/C, PtCo/KB, and PtCo/KB-NH₂ catalysts

- (A) Polarization and power density curves tested in H_2 /air fuel cells. Test conditions: 0.10 mg \cdot cm $^{-2}$ (anode/cathode Pt loadings), H_2 /air (500/1,000 sccm), 80°C, and 150 kPa (absolute) pressure.
- (B) Nyquist plots recorded at $0.60 \, \text{V}$ in $\, \text{H}_2 / \, \text{air}$ fuel cells corresponding to (A). The symbols are measured results, and the solid lines are fitted results using the inset equivalent circuit.
- (C) Power density at 0.67 V (in H₂/air fuel cells) and Pt utilization in MEAs.
- (D) H_2 /air polarization curves tested at BOL (solid symbols) and after (hollow symbols) 30,000 voltage cycles (0.60–0.95 V).
- (E) H₂/air fuel cell performance for PtCo/KB-NH₂ using a cathode loading of 0.20 mg_{Pt}•cm⁻² during 90,000 voltage cycles.
- (F) MA (at $0.9\,V_{iR-free}$) and voltage drops (at $0.8\,A\cdot cm^{-2}$) for MEAs after 30,000 voltage cycles. The purple and gray dashed lines indicate DOE targets for MA at BOL and end of life (EOL), respectively. The green dashed line indicates the DOE target for voltage drop.

brings the E_{OH^*} closer to the theoretical optimum value. The synergy between strain and ligand effects tuned E_{OH^*} to a just-right level for optimum ORR activity, which explained the excellent activity of PtCo/KB-NH₂ from a theoretical point of view.

Translating the excellent ORR activity into fuel cell performance remains a great challenge because of the insufficient Pt utilization and mass transport in the MEAs for traditional, highly active Pt-based catalysts. 3,39 MEA performance using PtCo/KB-NH₂ as the cathode catalyst was examined and compared with that using PtCo/KB and commercial Pt/C (Figure 5). In H₂/air fuel cells using a cathode loading of 0.10 mg_{Pt}·cm⁻², the MEA of PtCo/KB-NH₂ showed the best performance over the entire range of polarization curves, particularly in the low-voltage region dominated by mass transport resistance (Figure 5A). The MEA of PtCo/KB-NH₂ delivered an excellent MA (at 0.90 V_{iR-free}) of 0.691 A·mg_{Pt}⁻¹, which far exceeds that of PtCo/ KB (0.583 $A \cdot mg_{Pt}^{-1}$) and the DOE target (0.440 $A \cdot mg_{Pt}^{-1}$). In contrast, the MEA of commercial Pt/C exhibited a relatively low MA of 0.241 A·mg_{Pt}⁻¹. An extremely high current density of 480 mA·cm⁻² at 0.80 V was achieved using the MEA of PtCo/KB-NH₂, which is 1.6 times the DOE target (300 mA·cm⁻²). It is well known that MEA performance in the high-voltage region is dominated by the intrinsic activity of the cathode catalyst. The uniform and ultrafine L10-PtCo@Pt31 structure of PtCo catalysts enabled the superior activities in RDE and MEA tests. At an operating voltage of 0.67 V for practical fuel cell application, where performance is also limited by mass transport, the MEA of PtCo/KB-NH₂ exhibited a record-high power density of 0.96 W \cdot cm⁻² (Figures 5A and 5C). This rated power density is extremely closely

Matter Article



approaches the DOE target of 1.0 W·cm⁻² and outperforms that of PtCo/KB (0.89 $\rm W\cdot cm^{-2}$), commercial Pt/C (0.78 $\rm W\cdot cm^{-2}$), and other reported Pt-based catalysts (Table S1). In H₂/O₂ fuel cells (Figure S12A), a record-high maximum power density of 2.65 W·cm⁻² (at 0.45 V) was achieved using PtCo/KB-NH₂. To interpret the impressive MEA performance of the PtCo/KB-NH2 catalyst, electrochemical impedance spectra were recorded at 0.60 V in H₂/air fuel cells and fitted using an equivalent circuit described previously.⁵⁸ The Nyquist plots of these studied catalysts are compared in Figure 5B, and the fitted results are summarized in Table S3. The MEA of PtCo/KB-NH₂ had the smallest impedance arc, corresponding to the best MEA performance. MEA performance was dominated by cathode activation resistance ($R_{cathode}$) and mass transport resistance (R_{mt}) because they are much larger than ohmic resistance (R_{Ω}) and anode activation resistance ($R_{\rm anode}$) (Table S3). The $R_{cathode}$ of PtCo/KB-NH₂ (123.7 m Ω ·cm²) was lower than that of PtCo/KB (232.7 m Ω ·cm²) and commercial Pt/C (333.0 m Ω ·cm²), which agreed well with the intrinsic activities shown in Figure 3C. The R_{mt} of PtCo/KB-NH₂ (152.2 m Ω ·cm²) was also much lower than that of PtCo/KB (231.0 m Ω ·cm²) and commercial Pt/C (192.0 m $\Omega \cdot \text{cm}^2$), confirming that deposition of L1₀-PtCo nanoparticles primarily on the external surface of carbon supports reduced the $R_{\rm mt}$. The specific pore volume of the catalyst layer fabricated using PtCo/KB was higher than that using PtCo/KB-NH₂ (Figure S13C), ruling out the possibility that the lower $R_{\rm mt}$ is caused by a more porous structure of the corresponding catalyst layer. The Pt utilizations in MEAs were calculated by obtaining the relative values of the ECSA determined in the MEA (Figure S12B) to the ECSA determined in the RDE (Figure 3A). As shown in Figure 5C, PtCo/KB-NH₂ delivered an extremely high Pt utilization of 95.1% in the MEA because most of the PtCo nanoparticles are deposited on the external surface and, thus, accessible to proton-conducting ionomers. However, PtCo/KB and commercial Pt/C had lower Pt utilizations of 83.2% and 80.8% in MEAs, respectively, which are close to the reported commercial Pt/KB,⁵⁹ attributed to the fact that a large number of catalyst nanoparticles were embedded into the micropores and poorly accessible to ionomers. Therefore, PtCo/KB-NH2 enabled an enhanced accessible active area in the MEA and lowered the $R_{\rm mt}$, resulting in extremely high power performance.

Accelerated durability tests (ADTs) were performed by cycling the MEAs between 0.60 and 0.95 V for 30,000 voltage cycles using the DOE testing protocol. Apparently, the MEA of commercial Pt/C suffered severe degradation after the ADT (Figures 5D and 5F), showing an MA loss of 63.1% and voltage drop of 170 mV (at $0.8 \,\mathrm{A\cdot cm^{-2}}$). The MEAs of PtCo/KB-NH₂ and PtCo/KB demonstrated excellent durability with a voltage loss of 30 mV (at 0.8 A·cm⁻²) after the ADT, reaching the DOE target of 30 mV. The MA of PtCo/KB-NH₂ was maintained at a high level of 0.380 A·mg_{Pt}⁻¹ after the ADT, surpassing the DOE target of 0.264 A·mg_{Pt}⁻¹. As shown in Figure 5D, the retained MEA performance of PtCo/KB-NH₂ after the ADT is comparable with the initial MEA performance of commercial Pt/C. The MEA performance of PtCo/KB-NH2 reached nearly all DOE requirements for light-duty vehicles, indicating great potential of PtCo/KB-NH₂ for fuel cell applications. To investigate its potential application in heavy-duty vehicles, long-term performance was examined by cycling an MEA using a cathode loading of 0.20 mg_{Pt}·cm⁻² for 90,000 voltage cycles (Figure 5E). Initial MEA performance was enhanced because of the higher Pt loading, showing a power density of 1.02 W·cm⁻² (at 0.67 V). MEA performance decayed significantly for the first 30,000 cycles and then decayed slightly over the subsequent cycles. The current density at 0.70 V dropped from 1.31 to 0.83 A·cm⁻² after 90,000 cycles, indicating a current decay of 36.6%. Given the low testing pressure of 150 kPa_{abs}, the retained



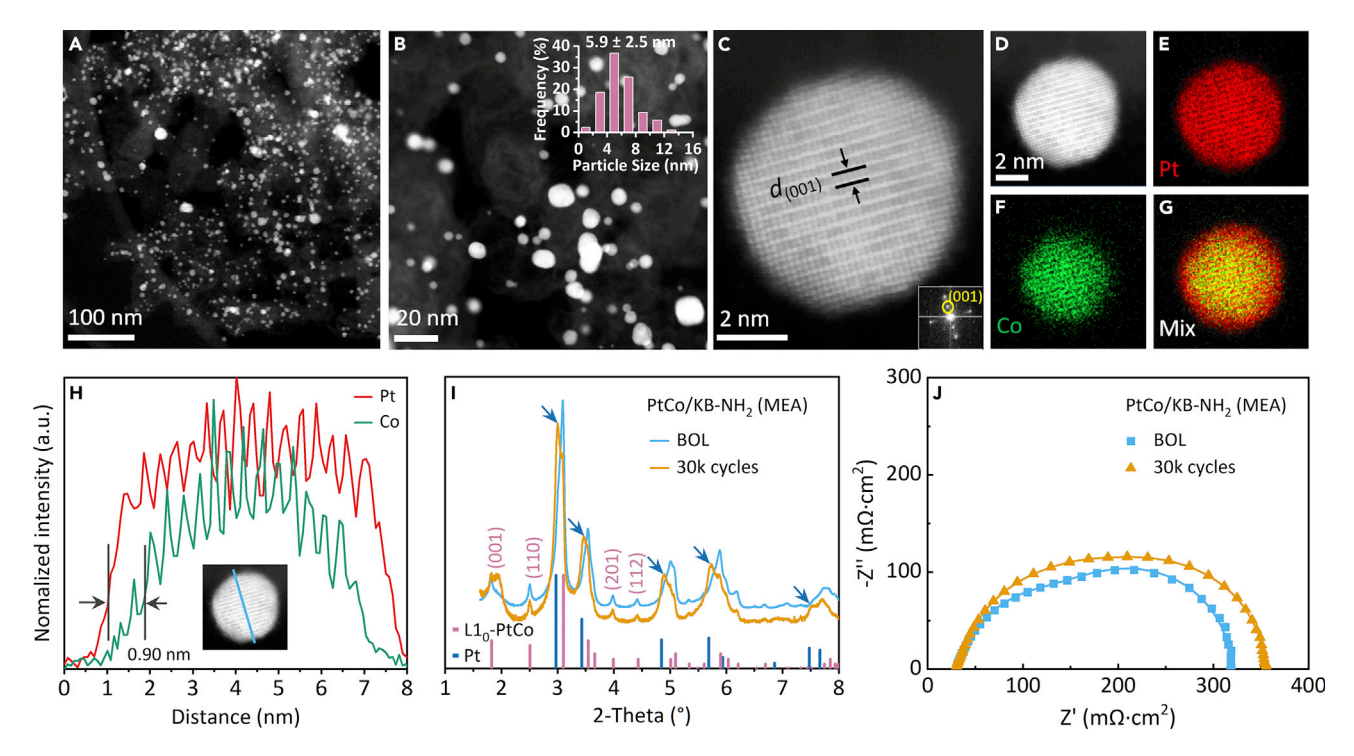


Figure 6. Characterization of the PtCo/KB-NH₂ catalyst after 30,000 voltage cycles

(A-H) Low-magnification STEM images (A and B), atomic-resolution STEM image (C), EDS elemental maps (D-G), and line-scan profile (H) of PtCo/KB-NH₂ nanoparticles after 30,000 voltage cycles (0.60–0.95 V) in the MEA. Insets in (B) and (C) show the corresponding particle size distribution and FFT pattern, respectively.

- (I) SHEXRD patterns of PtCo/KB-NH₂ recorded at BOL and after 30,000 voltage cycles in the MEA.
- (J) Nyquist plots recorded at 0.60 V in H_2 /air fuel cells at BOL and after 30,000 voltage cycles. Scale bars: 100 nm (A), 20 nm (B), and 2 nm (C and D).

current density of 0.83 $A \cdot cm^{-2}$ is a promising result but below the DOE target of 1.07 $A \cdot cm^{-2}$ for heavy-duty vehicles testing at 250 kPa_{abs}.⁶⁰

To gain insights into the catalyst degradation mechanisms, the microstructure of PtCo/KB-NH₂ in the MEA after 30,000 voltage cycles was examined in detail. The PtCo nanoparticles remained well dispersed on the carbon support after the ADT (Figures 6A and 6B), although the average particle size increased from 2.7 \pm 1.0 nm to 5.9 \pm 2.5 nm. In contrast, severe coarsening of Pt nanoparticles was observed for commercial Pt/C after the ADT, resulting in the average particle size increasing remarkably from 2.6 \pm 1.0 nm to 7.2 \pm 3.0 nm (Figure S14). Enhanced sintering resistance has been reported in the literature for Pt-Co, Pt-Ni, and Pt-Fe alloys compared with pure Pt catalysts, which may be due to the alloying metal (i.e., the anchor effects of alloying metals on the carbon supports). 13,61,62 Typical lattice fringes indexed to the (001) plane of the L1₀-PtCo structure and alternating Z-contrasts can be clearly identified in Figure 6C, indicating that the intermetallic structure is well preserved after the ADT, which definitely contributes to the excellent durability. The L1₀-PtCo nanoparticles exhibited a more defined core-shell structure after the ADT (Figures 6D-6H), showing a shell thickness of 0.90 nm, which is about 4 atomic Pt layers. Although a large amount of Co was observed to remain in the core structure after the ADT, the Co content in L1₀-PtCo nanoparticles decreased from 28 atom % (initial value) to 20 atom % (after the ADT) because of inevitable Co dissolution. The structure change was evidenced by the SHEXRD pattern after the ADT (Figure 6I), showing both diffraction peaks corresponding to





the L1₀-PtCo structure and emerging splitting peaks belonging to pure Pt. The R_{Ω} remained almost unchanged at 31.1 m Ω ·cm² after the ADT (Figure 6J), indicating that the dissolved Co did not lead to a significant increase in proton conduction resistance of the ionomer and membrane, which is consistent with the previous observations of the PtCo/C catalyst. 63 The effect of surface Co dissolution on the kinetic activity of L1₀-PtCo nanoparticles was studied by calculating the E_{OH*} on L1₀-PtCo@ Pt_{4L} (Figure S11C). Compared with L1₀-PtCo@Pt_{3L} (-1.241 eV), the E_{OH^*} varied slightly on L1₀-PtCo@Pt_{4L} (-1.237 eV) because the compressive strain remained almost unchanged at 3.42%, implying that surface Co dissolution may not result in a significant reduction in ORR activity. The surface contraction induced by the Pt-Co lattice mismatch faded away on nanoparticles with thicker shells, consistent with that observed on Pt@Pd nanoparticles.⁵⁷ Therefore, the MEA performance degradation could be mainly attributed to the reduction in active area caused by the increase in particle size. Future work is underway to prepare Pt-based intermetallic nanoparticles on other types of functionalized carbon supports to improve catalyst durability.

Conclusion

A simple and effective approach was developed to directly synthesize sub-3-nm L1₀-PtM nanoparticles on the external surface of carbon supports. The representative PtCo/KB-NH₂ nanoparticles exhibited 2-3 atomic Pt layers over the L1₀-PtCo core, showing excellent ORR activity (MA of 1.82 A·mg_{Pt}⁻¹) and durability (13.0% MA loss after 30,000 cycles) in RDE tests. DFT calculations revealed that a synergy of ligand effect and strain effect weakened the adsorption of oxygenated intermediates on PtCo/KB-NH₂ nanoparticles to a near-optimal value. Formation of L1₀ -PtCo structure and enhanced resistance against surface Pt oxidation in PtCo/KB-NH₂ were responsible for the superior durability. The excellent activity could be well translated into fuel cell performance because of the enhanced accessibility of $PtCo/KB-NH_2$ nanoparticles, resulting in high Pt utilization and low R_{mt} in the MEA. Using a low cathode loading of 0.10 mg_{Pt}·cm⁻², the MEA of PtCo/KB- NH_2 delivered a superior MA of 0.691 $A \cdot mg_{Pt}^{-1}$, a record-high power density of $0.96~\mathrm{W\cdot cm^{-2}}$ at $0.67~\mathrm{V}$, and only a 30 mV drop at $0.80~\mathrm{A\cdot cm^{-2}}$ after 30,000 voltage cycles. The current density could be maintained at a high level of 0.83 A·cm⁻² at 0.70 V (under a reasonably low-pressure testing condition of 150 kPa_{abs}) after 90,000 cycles, suggesting great potential for application of PtCo/KB-NH2 in heavy-duty vehicles. This work not only introduces a novel strategy to prepare uniform and ultrafine Pt-based intermetallic electrocatalysts but also provides an effective direction for overcoming the mass transport problem to achieve high-power fuel cells.

EXPERIMENTAL PROCEDURES

Resource availability

Lead contact

Further information and requests for resources and reagents should be directed to and will be fulfilled by the lead contact, J.X. (jianxie@iupui.edu).

Materials availability

This study did not generate new unique reagents.

Data and code availability

Requests for the data and code reported in this paper will be handled by the lead contact, J.X. (jianxie@iupui.edu).





Materials and chemicals

Materials used include KB EC300J (AkzoNobel Surface Chemistry), Vulcan (VC) XC-72 (Cabot), phenylenediamine (97%, Alfa Aesar), sulfuric acid (ACS reagent grade, Sigma-Aldrich), sodium nitrite (NaNO₂, 98%, Alfa Aesar), deionized water (18.2 M Ω ·cm), filtration membrane (0.025 μ m, Millipore), EG (certified grade, Fisher Chemical), chloroplatinic acid hexahydrate (H₂PtCl₆·6H₂O, 38-40% Pt, Strem Chemicals), anhydrous cobalt chloride (CoCl₂, 97%, Thermo Scientific), n-propanol (certified ACS, Fisher Scientific), ionomer solution (Nafion D520, Ion Power), ionomer solution (720 equivalent weight, Aquivion D72-25BS), Gore membrane (15 μ m, M820.15), 46.4 wt % Pt/C (TEC10E50E, Tanaka Kikinzoku Kogyo), 30 wt % Pt/C (Jiping New Energy), and gas diffusion layers (Sigracet 22BB, SGL Global).

Surface modification of carbon supports

Amino (–NH₂)-modified carbon supports were prepared using a diazonium reaction method based on our previous studies. 43,44 Briefly, 100 mg KB or 300 mg VC was dispersed into 100 mL of deionized water, followed by addition of 56 mg phenylenediamine and 30 μ L of concentrated sulfuric acid. After sonication for 30 min, 36 mL of a $1.0\,{\rm mg\cdot mL^{-1}}$ NaNO₂ aqueous solution was added dropwise into the suspension above. The reaction product was collected after magnetic stirring for 16 h at 60°C by filtering using deionized water on a 0.025- μ m filtration membrane. The resulting carbon was dried in a vacuum oven at 65°C for 12 h and then ground in an agate mortar. The amount of phenylenediamine introduced was calculated based on the surface area of carbon supports, and, according to previous studies, an excess of phenylenediamine was used to ensure maximum surface coverage of p-benzene-NH₂. 64,65

Synthesis of Pt/KB-NH₂

Pt nanoparticles were deposited on NH₂-modified KB (KB-NH₂) by reducing the Pt-precursor in an EG aqueous solution (60 vol % EG/40 vol % H₂O). Briefly, KB-NH₂ was dispersed in the EG aqueous solution, followed by addition of a certain amount of H₂ PtCl₆·6H₂O. The suspension was refluxed at 140°C for 6 h and then filtrated with deionized water and ethanol. Finally, Pt/KB-NH₂ was obtained after drying the product at 65°C for 12 h in a vacuum oven. For comparison, Pt/KB was also prepared using the same procedure, except that unmodified KB was used as support material. The nominal Pt loading was set at 8.0 wt %, and the detailed loading was determined using thermogravimetric analysis (TGA).

Synthesis of PtCo/KB-NH₂

100 mg of 8.0 wt % Pt/KB-NH₂ was initially dispersed in 50 mL of deionized water, followed by addition of 0.077 mmol of $H_2PtCl_6\cdot 6H_2O$ and 0.153 mmol of $CoCl_2$. After sonication for 30 min, the suspension was subjected to magnetic stirring at 60°C until the water fully evaporated to form a thick slurry. The slurry was dried in a vacuum oven at 65°C for 12 h and then ground in an agate mortar. The grounded powder was heated in a tube furnace at 400°C for 2 h and then at 650°C for another 6 h under flowing forming gas (5 vol % $H_2/95$ vol % Ar). The heating rate was maintained at 8°C·min⁻¹. The product was then treated in a 0.1 mol·L⁻¹ HClO₄ solution at 60°C for 6 h in air (Figure \$15), followed by heat treatment at 400°C for 1 h under flowing forming gas. The Pt loading for PtCo/KB-NH₂ was determined to be 24.0 wt % using ICP-AES.

Synthesis of PtCo/KB

100 mg of 8.0 wt % Pt/KB was initially dispersed in 50 mL of deionized water, followed by addition of 0.128 mmol of $H_2PtCl_6 \cdot 6H_2O$ and 0.220 mmol of $CoCl_2$, and





the subsequent process was the same as that for PtCo/KB-NH₂. The Pt loading for PtCo/KB was determined to be 23.5 wt % using ICP-AES.

Synthesis of PtCo/KB-traditional

PtCo/KB-traditional was prepared utilizing the traditional impregnation method without seed mediation and carbon modification. Initially, 85 mg kB was dispersed in 50 mL of deionized water, followed by addition of 0.154 mmol of H₂PtCl₆·6H₂O and 0.201 mmol of $CoCl_2$, and the subsequent procedure was the same as that for PtCo/KB-NH₂. The Pt loading of PtCo/KB-traditional was determined to be 24.6 wt % using ICP-AES.

Physical characterization

Nitrogen adsorption/desorption isotherms were measured using an automated gas sorption analyzer (Autosorb-iQ, Quantachrome Instrument), and specific surface areas were determined using the BET method. By assuming a slit-shaped pore structure, the pore size distribution was evaluated using non-local DFT (NLDFT). Based on our previous study, mercury intrusion porosimetry measurements were performed on an AutoPore IV 9520 analyzer (Micromeritics). 58 TGA was carried out by heating powder samples to 800°C at a rate of 10°C⋅min⁻¹ under an air (or Ar) atmosphere using a thermal analyzer (SDT Q600, TA Instruments). The detailed Pt loadings for PtM catalysts were determined using ICP-AES (Teledyne Leeman Labs). XPS measurements were performed on a PHI 5000 VersaProbe II system (Physical Electronics) using an Al K α radiation (h ν = 1486.6 eV) beam (100 μ m, 25 W). XAS was performed using transmission mode on beamline 20-BM-B at the Advanced Photon Source (Argonne National Laboratory). XAS data processing and EXAFS fitting were performed using the Athena and Artemis software packages.

STEM and EDS measurements were carried out using an aberration-corrected JEOL NEOARM electron microscope, and a JEOL JEM-F200 was used for TEM. Particle size distributions were obtained by randomly measuring more than 300 nanoparticles in corresponding TEM and STEM images. To determine the locations of catalyst nanoparticles over the carbon surface, STEM images were acquired simultaneously in SE and HAADF modes. The SE image reveals catalyst nanoparticles located only on the external surface of carbon supports, whereas catalyst nanoparticles on the external and internal surfaces of carbon supports are visible in the HADDF image. 41,66 When detected in SE mode, the nanoparticles are assumed to be similar on the front and back sides of the catalyst because of the homogeneous distribution and fixed sample holder. Comparing SE and HADDF images enables separation of nanoparticles positioned on the internal and external surfaces of the carbon support, respectively. The particle localization results for PtCo/KB-NH₂ and PtCo/KB catalysts are based on analysis of more than 200 nanoparticles from several SE/HADDF images. The proportion of nanoparticles exposed on the external carbon surface is calculated from the counted particles.

SHEXRD was carried out on the beamline 11-ID-C at the Advanced Photon Source(Argonne National Laboratory). A high-energy X-ray with a beam size of 0.2×0.2 mm and a wavelength of 0.1173 Å was used. Diffraction patterns were collected using a PerkinElmer area detector in the Laue diffraction geometry, placed 1,800 mm from the sample. In situ SHEXRD was performed on the same beamline during the heat treatment. The high penetration and low absorption of SHEXRD are beneficial for observing tiny phase changes that are usually invisible from labscale XRD. Dry powders of 8.0 wt % Pt/KB-NH₂ impregnated with Pt and Co precursors were used for the in situ heat treatment test. The sample was pressed into a





pellet approximately 1 mm thick and then placed between a ceramic can and a platinum cover with a hole (D = 1 mm) in the center of the ceramic can and the platinum cover. The sample was heated at 400°C for 2 h and then at 650°C for 3 h under forming gas (10 vol % $H_2/90$ vol % Ar). The heating rate was kept constant at $8^{\circ}\text{C} \cdot \text{min}^{-1}$. The diffraction data were collected every 60 s and calibrated using a standard CeO_2 sample.

Electrochemical characterization

Electrochemical measurements were performed utilizing a typical three-electrode system. A glassy carbon (0.196 cm²) rotating disc electrode (RDE; Pine Research Instrumentation), a Pt wire (Pine Research Instrumentation), and a reversible hydrogen electrode (RHE; HydroFlex) were used as working, counter, and reference electrodes, respectively. All potentials in this work are reported with respect to RHE. The catalyst ink was prepared by ultrasonically dispersing 5 mg catalysts into a mixed solution of 4 mL deionized water, 1 mL iso-propanol, and 10 μ L Nafion solution (5 wt % D520). The ink was uniformly deposited onto a polished glassy carbon electrode with a designed Pt loading of 12 μ g·cm² and then dried in air at room temperature.

Electrochemical measurements were performed in 0.1 mol L $^{-1}$ HClO $_4$ electrolytes at room temperature using an electrochemical potentiostat (VSP, Bio-Logic). Prior to electrochemical tests, the electrodes were activated by cycling potential between 0.05 and 1.20 V at 500 mV·s $^{-1}$ for 50 cycles in N $_2$ -saturated electrolytes. CV curves were measured by scanning potential from 0.05–1.10 V at 20 mV·s $^{-1}$ in N $_2$ -saturated electrolytes. ORR polarization curves were recorded in O $_2$ -saturated electrolytes at a rotation rate of 1,600 rpm and a sweep rate of 20 mV·s $^{-1}$ with iR correction. Catalyst durability tests were performed by conducting 30,000 potential cycles between 0.60 and 0.95 V (a trapezoidal wave with 0.5-s rise time and 2.5-s hold time) in N $_2$ -saturated electrolytes. CO stripping tests were performed by bubbling CO into a 0.1 mol·L $^{-1}$ HClO $_4$ electrolyte and holding potential at 0.07 V for 30 min, followed by bubbling N $_2$ into the electrolyte for 30 min. CO stripping curves were then collected by scanning potential from 0.05–1.10 V at 20 mV·s $^{-1}$. ECSAs were calculated by integrating the areas of hydrogen adsorption regions (CV curves) or CO desorption regions (CO stripping curves).

Fuel cell fabrication and testing

MEA was fabricated by ultrasonically spraying cathode/anode catalyst ink onto a 15- μ m membrane (Gore M820.15) using an ExactCoat spray coating system (Sono-Tek). The as-prepared PtCo/KB-NH₂, PtCo/KB, or commercial 46.4 wt % Pt/C (TEC10E50E, Tanaka Kikinzoku Kogyo) was dispersed into an n-propanol aqueous solution (10 wt % n-PA/90 wt % H₂O) with the ionomer solution (Aquivion D72-25BS) as cathode catalyst ink. The solid content was 2.0 mg·mL⁻¹, and weight ratios of ionomer/carbon (I/C) for PtCo/KB-NH₂ and PtCo/KB were controlled to be 0.50 and 0.60 (Figure S16), respectively. Commercial 30 wt % Pt/C (Jiping New Energy) was used as an anode catalyst with an I/C ratio of 0.45. All catalyst inks were homogenized using an ultrasonic bath for 30 min and a sonic dismembrator for 4 min. Catalyst-coated membranes (CCMs) were sandwiched between two gas diffusion layers without hot pressing.

MEAs with an active area of $5.0~\rm cm^2$ were assembled into fuel cell hardware with differential flow channels and tested on a model 850e fuel cell system (Scribner Associates). The differential flow channels enable use of high flow rates without increasing pressure (Figure S17). The MEAs were first activated (break-in) in potential step mode from 0.35– $0.75~\rm V$ (0.05-V increments every 5 min) for 16 h using H₂/air





flow rates of 200/400 standard cubic centimeters per minute (sccm) and 100% relative humidity (RH). After break-in, a recovery step was applied by holding the cell voltage at 0.10 V for 2 h at 30°C under H₂/air (200/400 sccm) as described previously.⁶⁷ The ECSA values were then obtained using the hydrogen adsorption/ desorption method by employing CV curves between 0.05 and 0.60 V at a scan rate of 20 mV·s⁻¹ at a cell temperature of 30°C under 150-kPa_{abs} pressure. Prior to ECSA tests, the cathode was purged with N2 until the open circuit voltage dropped below 0.15 V. The CV curves were measured using an electrochemical workstation (Solartron 1287BZ, Ametek). The gases of the anode and cathode were humidified at 80°C during voltage recovery and ECSA measurements.

Fuel cell polarization curves were recorded using potential step mode with 50 mV/point by holding for 1 min at each point under 150-kPa $_{abs}$ pressure. The H_2 /O₂ polarization curves were measured at constant flow rates of 200/400 sccm (100%/100% RH). The H₂/air polarization curves were recorded at constant flow rates of 500/1,000 sccm (100% RH/75% RH) (Figure S18). The electrochemical impedance spectra were collected at 0.60 V by scanning frequency from 10,000-0.1 Hz during the H₂/air fuel cell tests. Mass activities were determined by measuring current in 150 kPa_{abs} H_2/O_2 (80°C, 100% RH, 500/2,000 sccm) at 0.9 $V_{iR-free}$ (holding for 15 min and recording the average current for the last 1 min) with correction for measured H₂ crossover, according to the DOE protocol. ADTs were carried out by cycling the voltage from 0.60-0.95 V using a trapezoidal wave with 0.5-s rise time and 2.5-s hold time under H_2/N_2 (80°C, 100% RH, 100/100 sccm).

Computational methods

The first-principles DFT calculations were done by the spin-polarized Vienna Ab Initio Simulation Package (VASP)⁶⁸⁻⁷⁰ using the Perdew-Burke-Ernzerhof (PBE)⁷¹ functional to describe electronic exchange and correlation in the Brillouin zone, which includes only the gamma point with a smearing width of 0.2 eV. The atomic coordinates were optimized using the RMM-DIIS ionic relaxation algorithm⁶⁹ with a plane-wave cutoff energy of 400 eV until the Hellman-Feynman force is less than 0.02 eV/Å on each ion and the electronic structure converged to a level of 1×10^{-6} eV. A semispherical core-shell model of L1₀-PtCo@Pt_{3L} was used to simulate PtCo/KB-NH₂ nanoparticles. The semispherical model with a radius of 1.3 nm consisted of 3 Pt atomic layers over a bulk L1₀-PtCo alloy core in fct structure. The model is constructed in an isolated space where a minimum of 2.5 nm vacuum is separated between adjacent units. To optimize the structure, the bottom of the semisphere was restrained to be planar to systematically present the full-sphere nanoparticle. The 4 \times 4 slab model of L1₀-PtCo@Pt₃₁ (111), containing a three-layer Pt (111) surface over the L1₀-PtCo base, was used to calculate E_{OH^*} by applying a 3.42% compressive strain obtained from the (111) facet of the semispherical model because of the limitation of computing resources. The dissolution potential of surface Pt atoms was calculated using the slab model with the strain obtained from the corresponding semispherical model, according to a previous study.⁷²

SUPPLEMENTAL INFORMATION

Supplemental information can be found online at https://doi.org/10.1016/j.matt. 2022.12.011.

ACKNOWLEDGMENTS

This work was partially supported by the Hydrogen and Fuel Cell Technologies Office, Office of Energy Efficiency and Renewable Energy, U.S. Department of Energy





(DOE). This research utilized resources of the Advanced Photon Source, an Office of Science User Facility operated by Argonne National Laboratory for the U.S. DOE Office of Science under contract DE-AC02-06CH11357. The Center for Nanophase Materials Sciences (CNMS), which is a U.S. DOE Office of Science User Facility at Oak Ridge National Laboratory, and the Singh Center for Nanotechnology at the University of Pennsylvania, which is supported by the NSF National Nanotechnology Coordinated Infrastructure Program under grant NNCI-1542153 and by the NSF through the University of Pennsylvania Materials Research Science and Engineering Center (MRSEC) (DMR-1720530), carried out the electron microscopy work. A.C.F. acknowledges support from IMASC, an Energy Frontier Research Center funded by the U.S. DOE Office of Science. S.J. and E.A.S. acknowledge support from the Center for Hybrid Approaches in Solar Energy to Liquid Fuels (CHASE), an Energy Innovation Hub funded by the U.S. DOE Office of Science, Office of Basic Energy Sciences under award DE-SC0021173. Theoretical studies were performed at Brookhaven National Laboratory and supported by the Chemical Sciences, Geosciences, and Biosciences Division, U.S. DOE Office of Basic Energy Science, under contract DE-SC0012704. The calculations performed in this work used computational resources at the Center for Functional Nanomaterials (CFN) and the Scientific Data and Computing Center, a component of the Computational Science Initiative, at Brookhaven National Laboratory, under contract DE-SC0012704 and at Stony Brook University, which was funded by a National Science Foundation grant (1531492). The authors gratefully acknowledge help from the Post Test Facility at Argonne National Laboratory, supported by the U.S. DOE Vehicle Technologies Office under contract DE-AC02-06CH11357.

AUTHOR CONTRIBUTIONS

Conceptualization, Q.G., J.X. and H.Y.; methodology, Q.G.; investigation, Q.G., H.Y., S.J., E.A.S., A.C.F., D.A.C., M.S., Y.R., Z.Y., and C.-J.S.; formal analysis, Q.G. and H.Y.; data curation, Q.G.; visualization, Q.G. and H.Z.; writing - original draft, Q.G. and H.Z.; software, H.Z.; writing - review & editing, J.X., E.A.S., D.A.C., and P.L.; resources, Y.Y. and G.M.F.; funding acquisition, J.X.; supervision, J.X.

DECLARATION OF INTERESTS

The authors declare no competing interests.

Received: August 11, 2022 Revised: November 5, 2022 Accepted: December 16, 2022 Published: January 12, 2023

REFERENCES

- 1. Nie, Y., Li, L., and Wei, Z. (2021). Achievements in Pt nanoalloy oxygen reduction reaction catalysts: strain engineering, stability and atom utilization efficiency. Chem. Commun. 57, 12898-12913. https://doi.org/10.1039/ d1cc05534h.
- 2. Wang, X.X., Swihart, M.T., and Wu, G. (2019). Achievements, challenges and perspectives on cathode catalysts in proton exchange membrane fuel cells for transportation. Nat. Catal. 2, 578-589. https://doi.org/10.1038/ s41929-019-0304-9
- 3. Kongkanand, A., and Mathias, M.F. (2016). The priority and challenge of high-power

- performance of low-platinum protonexchange membrane fuel cells. J. Phys. Chem. Lett. 7, 1127-1137. https://doi.org/10.1021/ acs.jpclett.6b00216.
- 4. Shao, M., Chang, Q., Dodelet, J.P., and Chenitz, R. (2016). Recent advances in electrocatalysts for oxygen reduction reaction. Chem. Rev. 116, 3594-3657. https://doi.org/10. 1021/acs.chemrev.5b00462.
- 5. Nie, Y., Li, L., and Wei, Z. (2015). Recent advancements in Pt and Pt-free catalysts for oxygen reduction reaction. Chem. Soc. Rev. 44, 2168-2201. https://doi.org/10.1039/ c4cs00484a
- 6. Bing, Y., Liu, H., Zhang, L., Ghosh, D., and Zhang, J. (2010). Nanostructured Pt-alloy electrocatalysts for PEM fuel cell oxygen reduction reaction. Chem. Soc. Rev. 39, 2184-2202. https://doi.org/10.1039/b912552c
- 7. Kulkarni, A., Siahrostami, S., Patel, A., and Nørskov, J.K. (2018). Understanding catalytic activity trends in the oxyger reduction reaction. Chem. Rev. 118, 2302-2312. https://doi.org/10.1021/acs.chemrev. 7b00488
- 8. Stamenkovic, V., Mun, B.S., Mayrhofer, K.J.J., Ross, P.N., Markovic, N.M., Rossmeisl, J., Greeley, J., and Nørskov, J.K. (2006). Changing

Matter Article



- the activity of electrocatalysts for oxygen reduction by tuning the surface electronic structure. Angew. Chem. Int. Ed. Engl. 45, 2897-2901. https://doi.org/10.1002/anie
- 9. Greeley, J., Stephens, I.E.L., Bondarenko, A.S., Johansson, T.P., Hansen, H.A., Jaramillo, T.F., Rossmeisl, J., Chorkendorff, I., and Nørskov, J.K. (2009). Alloys of platinum and early transition metals as oxygen reduction electrocatalysts. Nat. Chem. 1, 552-556. https://doi.org/10.1038/NCHEM.367.
- Strasser, P., Koh, S., Anniyev, T., Greeley, J., More, K., Yu, C., Liu, Z., Kaya, S., Nordlund, D., Ogasawara, H., et al. (2010). Lattice-strain control of the activity in dealloyed core-shell fuel cell catalysts. Nat. Chem. 2, 454-460. https://doi.org/10.1038/NCHEM.623
- 11. Stephens, I.E.L., Bondarenko, A.S., Grønbjerg, U., Rossmeisl, J., and Chorkendorff, I. (2012). Understanding the electrocatalysis of oxygen reduction on platinum and its alloys. Energy Environ. Sci. 5, 6744–6762. https://doi.org/10. 1039/c2ee03590a.
- Shao, Y., Yin, G., and Gao, Y. (2007). Understanding and approaches for the durability issues of Pt-based catalysts for PEM fuel cell. J. Power Sources 171, 558–566. https://doi.org/10.1016/j.jpowsour.2007
- 13. Colón-Mercado, H.R., and Popov, B.N. (2006). Stability of platinum based alloy cathode catalysts in PEM fuel cells. J. Power Sources 155, 253-263. https://doi.org/10.1016/j. jpowsour.2005.05.011.
- 14. Wu, J., Yuan, X.Z., Martin, J.J., Wang, H., Zhang, J., Shen, J., Wu, S., and Merida, W. (2008). A review of PEM fuel cell durability: degradation mechanisms and mitigation strategies. J. Power Sources 184, 104-119. https://doi.org/10.1016/j.jpowsour.2008
- 15. Cullen, D.A., Neyerlin, K.C., Ahluwalia, R.K., Mukundan, R., More, K.L., Borup, R.L., Weber, A.Z., Myers, D.J., and Kusoglu, A. (2021). New roads and challenges for fuel cells in heavyduty transportation. Nat. Energy *6*, 462–474. https://doi.org/10.1038/s41560-021-00775-z.
- 16. Liang, J., Ma, F., Hwang, S., Wang, X., Sokolowski, J., Li, Q., Wu, G., and Su, D. (2019). Atomic arrangement engineering of metallic nanocrystals for energy-conversion electrocatalysis. Joule 3, 956-991. https://doi. org/10.1016/j.joule.2019.03.014.
- 17. Gamler, J.T.L., Ashberry, H.M., Skrabalak, S.E., and Koczkur, K.M. (2018). Random alloyed versus intermetallic nanoparticles: a comparison of electrocatalytic performance. Adv. Mater. 30, 1801563. https://doi.org/10. 1002/adma.201801563.
- 18. Li, Q., Wu, L., Wu, G., Su, D., Lv, H., Zhang, S., Zhu, W., Casimir, A., Zhu, H., Mendoza-Garcia, A., and Sun, S. (2015). New approach to fully ordered fct-FePt nanoparticles for much enhanced electrocatalysis in acid. Nano Lett. 15, 2468-2473. https://doi.org/10.1021/acs nanolett.5b00320.
- 19. Li, J., Sharma, S., Liu, X., Pan, Y.-T., Spendelow, J.S., Chi, M., Jia, Y., Zhang, P., Cullen, D.A., Xi, Z., et al. (2019). Hard-magnet L1₀-CoPt

- nanoparticles advance fuel cell catalysis. Joule 3, 124-135. https://doi.org/10.1016/j.joule. 2018.09.016.
- 20. Li, J., Xi, Z., Pan, Y.T., Spendelow, J.S., Duchesne, P.N., Su, D., Li, Q., Yu, C., Yin, Z., Shen, B., et al. (2018). Fe Stabilization by intermetallic $L1_0$ -FePt and Pt catalysis enhancement in L1₀-FePt/Pt nanoparticles for efficient oxygen reduction reaction in fuel cells. J. Am. Chem. Soc. 140, 2926–2932. https://doi. org/10.1021/jacs.7b12829
- 21. Kim, H.Y., and Joo, S.H. (2020). Recent advances in nanostructured intermetallic electrocatalysts for renewable energy conversion reactions. J. Mater. Chem. 8, 8195-8217. https://doi.org/10.1039/D0TA01809K
- 22. Zou, L., Fan, J., Zhou, Y., Wang, C., Li, J., Zou, Z., and Yang, H. (2015). Conversion of PtNi alloy from disordered to ordered for enhanced activity and durability in methanol-tolerant oxygen reduction reactions. Nano Res. 8, 2777-2788. https://doi.org/10.1007/s12274-015-
- 23. Shao, M., Peles, A., and Shoemaker, K. (2011). Electrocatalysis on platinum nanoparticles: particle size effect on oxygen reduction reaction activity. Nano Lett. 11, 3714-3719. https://doi.org/10.1021/nl2017459.
- 24. Tritsaris, G.A., Greeley, J., Rossmeisl, J., and Nørskov, J.K. (2011). Atomic-scale modeling of particle size effects for the oxygen reduction reaction on Pt. Catal. Lett. 141, 909-913. https://doi.org/10.1007/s10562-011-0637-8.
- 25. Kim, J., Lee, Y., and Sun, S. (2010). Structurally ordered FePt nanoparticles and their enhanced catalysis for oxygen reduction reaction. J. Am. Chem. Soc. 132, 4996–4997. https://doi.org/10.1021/ja1009629.
- 26. Lee, J.D., Jishkariani, D., Zhao, Y., Najmr, S., Rosen, D., Kikkawa, J.M., Stach, E.A., and Murray, C.B. (2019). Tuning the electrocatalytic oxygen reduction reaction activity of Pt-Co nanocrystals by cobalt concentration with atomic-scale understanding. ACS Appl. Mater. Interfaces 11, 26789-26797. https://doi.org/10. 1021/acsami.9b06346.
- 27. Liang, J., Li, N., Zhao, Z., Ma, L., Wang, X., Li, S., Liu, X., Wang, T., Du, Y., Lu, G., et al. (2019). Tungsten-doped L1₀-PtCo ultrasmall nanoparticles as a high-performance fuel cell cathode. Angew. Chem. Int. Ed. Engl. 58, 15471-15477. https://doi.org/10.1002/anie.
- 28. Li, J., Sharma, S., Wei, K., Chen, Z., Morris, D., Lin, H., Zeng, C., Chi, M., Yin, Z., Muzzio, M., et al. (2020). Anisotropic strain tuning of $L1_0$ ternary nanoparticles for oxygen reduction. J. Am. Chem. Soc. 142, 19209-19216. https:// doi.org/10.1021/jacs.0c08962
- 29. Xie, M., Lyu, Z., Chen, R., Shen, M., Cao, Z., and Xia, Y. (2021). Pt-Co@Pt octahedral nanocrystals: enhancing their activity and durability toward oxygen reduction with an intermetallic core and an ultrathin shell. J. Am. Chem. Soc. 143, 8509–8518. https://doi.org/10. 1021/jacs.1c04160.
- 30. Li, J., Jilani, S.Z., Lin, H., Liu, X., Wei, K., Jia, Y., Zhang, P., Chi, M., Tong, Y.J., Xi, Z., and Sun, S. (2019). Ternary CoPtAu nanoparticles as a general catalyst for highly efficient electro-

- oxidation of liquid fuels. Angew. Chem. Int. Ed. Engl. *58*, 11527–11533. https://doi.org/10. 1002/ange.201906137.
- Wang, T., Liang, J., Zhao, Z., Li, S., Lu, G., Xia, Z., Wang, C., Luo, J., Han, J., Ma, C., et al. (2019). Sub-6 nm fully ordered L1₀-Pt-Ni-Co nanoparticles enhance oxygen reduction via Co doping induced ferromagnetism enhancement and optimized surface strain. Adv. Energy Mater. 9, 1803771. https://doi.org/ 10.1002/aenm.201803771.
- 32. Liang, J., Zhao, Z., Li, N., Wang, X., Li, S., Liu, X., Wang, T., Lu, G., Wang, D., Hwang, B., et al. (2020). Biaxial strains mediated oxygen reduction electrocatalysis on fenton reaction resistant L1₀-PtZn fuel cell cathode. Adv. Energy Mater. 10, 2000179. https://doi.org/10. 1002/aenm 202000179
- 33. Qi, Z., Xiao, C., Liu, C., Goh, T.W., Zhou, L., Maligal-Ganesh, R., Pei, Y., Li, X., Curtiss, L.A., and Huang, W. (2017). Sub-4 nm PtZn intermetallic nanoparticles for enhanced mass and specific activities in catalytic electrooxidation reaction. J. Ám. Chem. Soc. 139, 4762-4768. https://doi.org/10.1021/jacs.
- 34. Du, X.X., He, Y., Wang, X.X., and Wang, J.N. (2016). Fine-grained and fully ordered intermetallic PtFe catalysts with largely enhanced catalytic activity and durability. Energy Environ. Sci. 9, 2623-2632. https://doi. org/10.1039/c6ee01204c.
- Yoo, T.Y., Yoo, J.M., Sinha, A.K., Bootharaju, M.S., Jung, E., Lee, H.S., Lee, B.H., Kim, J., Antink, W.H., Kim, Y.M., et al. (2020). Direct synthesis of intermetallic platinum-alloy nanoparticles highly loaded on carbon supports for efficient electrocatalysis. J. Am. Chem. Soc. 142, 14190-14200. https://doi.org/ 10.1021/jacs.0c05140.
- 36. Jung, W.S., Lee, W.H., Oh, H.-S., and Popov, B.N. (2020). Highly stable and ordered intermetallic PtCo alloy catalyst supported on graphitized carbon containing Co@CN for oxygen reduction reaction. J. Mater. Chem. 8, 19833–19842. https://doi.org/10.1039/ d0ta05182a
- 37. Chung, D.Y., Jun, S.W., Yoon, G., Kwon, S.G., Shin, D.Y., Seo, P., Yoo, J.M., Shin, H., Chung, Y.H., Kim, H., et al. (2015). Highly durable and active PtFe nanocatalyst for electrochemical oxygen reduction reaction. J. Am. Chem. Soc. 137, 15478-15485. https://doi.org/10.1021/ iacs.5b09653.
- 38. He, S., Liu, Y., Zhan, H., and Guan, L. (2021). Direct thermal annealing synthesis of ordered Pt alloy nanoparticles coated with a thin N-doped carbon shell for the oxygen reduction reaction. ACS Catal. 11, 9355-9365. https://doi. org/10.1021/acscatal.1c02434
- 39. Fan, T., Zhang, Y., Fan, J.S., Yuan, W., Lin, Z., Xu, S., Wang, H., and Li, H. (2021). Bridging the gap between highly active oxygen reduction reaction catalysts and effective catalyst layers for proton exchange membrane fuel cells. Nat. Energy 6, 475–486. https://doi.org/10.1038/ s41560-021-00824-7.
- 40. Yarlagadda, V., Carpenter, M.K., Moylan, T.E., Kukreja, R.S., Koestner, R., Gu, W., Thompson, L., and Kongkanand, A. (2018). Boosting fuel cell performance with accessible carbon





- mesopores. ACS Energy Lett. 3, 618-621. https://doi.org/10.1021/acsenergylett.
- 41. Park, Y.-C., Tokiwa, H., Kakinuma, K., Watanabe, M., and Uchida, M. (2016). Effects of carbon supports on Pt distribution, ionomer coverage and cathode performance for polymer electrolyte fuel cells. J. Power Sources 315, 179-191. https://doi.org/10.1016/j. jpowsour.2016.02.091.
- 42. Ott, S., Orfanidi, A., Schmies, H., Anke, B., Nong, H.N., Hübner, J., Gernert, U., Gliech, M., Lerch, M., and Strasser, P. (2020). Ionomer distribution control in porous carbonsupported catalyst layers for high-power and low Pt-loaded proton exchange membrane fuel cells. Nat. Mater. 19, 77-85. https://doi. org/10.1038/s41563-019-0487-0.
- 43. Xin, L., Yang, F., Rasouli, S., Qiu, Y., Li, Z.-F., Uzunoglu, A., Sun, C.-J., Liu, Y., Ferreira, P., Li, W., et al. (2016). Understanding Pt nanoparticle anchoring on graphene supports through surface functionalization. ACS Catal. 6, 2642-2653. https://doi.org/10.1021/acscatal.
- 44. Yang, F., Xin, L., Uzunoglu, A., Qiu, Y., Stanciu, L., Ilavsky, J., Li, W., and Xie, J. (2017). Investigation of the interaction between nafion ionomer and surface functionalized carbon black using both ultrasmall angle X-ray scattering and Cryo-TEM. ACS Appl. Mater. Interfaces 9, 6530-6538. https://doi.org/10. 1021/acsami.6b12949.
- 45. Fang, Z., Lee, M.S., Kim, J.Y., Kim, J.H., and Fuller, T.F. (2020). The effect of carbon support surface functionalization on PEM fuel cell performance, durability, and ionomer coverage in the catalyst layer. J. Electrochem. Soc. 167, 064506. https://doi.org/10.1149/ 1945-7111/ab7ea3.
- 46. Stamenkovic, V.R., Fowler, B., Mun, B.S., Wang, G., Ross, P.N., Lucas, C.A., and Marković, N.M. (2007). Improved oxygen reduction activity on Pt₃Ni (111) via increased surface site availability. Science 315, 493-497. https://doi. org/10.1126/science.1135941.
- 47. Lim, B., Lu, X., Jiang, M., Camargo, P.H.C., Cho, E.C., Lee, E.P., and Xia, Y. (2008). Facile Synthesis of highly faceted multioctahedral Pt nanocrystals through controlled overgrowth. Nano Lett. 8, 4043-4047. https://doi.org/10.
- 48. Marković, N., Adžić, R., Cahan, B.D., and Yeager, E.B. (1994). Structural effects in electrocatalysis: oxygen reduction on platinum low index single-crystal surfaces in perchloric acid solutions. J. Electroanal. Chem. 377, 249-259. https://doi.org/10.1016/0022 0728(94)03467-2.
- 49. Takahashi, Y.K., Koyama, T., Ohnuma, M., Ohkubo, T., and Hono, K. (2004). Size dependence of ordering in FePt nanoparticles. J. Appl. Phys. 95, 2690–2696. https://doi.org/ 10.1063/1.1643187.
- 50. van der Vliet, D.F., Wang, C., Li, D., Paulikas, A.P., Greeley, J., Rankin, R.B., Strmcnik, D., Tripkovic, D., Markovic, N.M., and Stamenkovic, V.R. (2012). Unique electrochemical adsorption properties of Pt-

- skin surfaces. Angew. Chem. Int. Ed. Engl. 51, 3139-3142. https://doi.org/10.1002/anie 201107668.
- 51. Rudi, S., Cui, C., Gan, L., and Strasser, P. (2014). Comparative study of the electrocatalytically active surface areas (ECSAs) of Pt alloy nanoparticles evaluated by H_{upd} and COstripping voltammetry. Electrocatalysis 5, 408-418. https://doi.org/10.1007/s12678-014-0205-2.
- 52. Łukaszewski, M.; Warsaw University Department of Chemistry Pasteura 1 02-093 Warsaw Poland, and Czerwiński, A. (2016). Electrochemical methods of real surface area determination of noble metal electrodes-an overview. Int. J. Electrochem. Sci. 11, 4442-4469. https://doi.org/10.20964/2016.06.71
- 53. Qiao, Z., Wang, C., Li, C., Zeng, Y., Hwang, S., Li, B., Karakalos, S., Park, J., Kropf, A.J., Wegener, E.C., et al. (2021). Atomically dispersed single iron sites for promoting Pt and Pt₃Co fuel cell catalysts: performance and durability improvements. Energy Environ. Sci. 14, 4948-4960. https://doi.org/10.1039/ d1ee01675j.
- 54. Cheng, Q., Yang, S., Fu, C., Zou, L., Zou, Z. Jiang, Z., Zhang, J., and Yang, H. (2022). High-loaded sub-6 nm PtCo intermetallic compounds with highly efficient performance expression in PEMFCs. Energy Environ. Sci. 15, 278-286. https://doi.org/10.1039/ D1EE02530A.
- 55. Wang, X.X., Hwang, S., Pan, Y.T., Chen, K., He, Y., Karakalos, S., Zhang, H., Spendelow, J.S., Su, D., and Wu, G. (2018). Ordered Pt₃Co intermetallic nanoparticles derived from metalorganic frameworks for oxygen reduction. Nano Lett. 18, 4163-4171. https://doi.org/10. 1021/acs.nanolett.8b00978.
- 56. Liu, S., White, M.G., and Liu, P. (2016). Mechanism of oxygen reduction reaction on Pt(111) in alkaline solution: importance of chemisorbed water on surface. J. Phys. Chem. C 120, 15288-15298. https://doi.org/10.1021/ acs.jpcc.6b05126.
- 57. Wang, J.X., Inada, H., Wu, L., Zhu, Y., Choi, Y., Liu, P., Zhou, W.-P., and Adzic, R.R. (2009). Oxygen reduction on well-defined core-shell nanocatalysts: particle size, facet, and Pt shell thickness effects. J. Am. Chem. Soc. 131, 17298-17302. https://doi.org/10.1021/
- 58. Gong, Q., Li, C., Liu, Y., Ilavsky, J., Guo, F., Cheng, X., and Xie, J. (2021). Effects of ink formulation on construction of catalyst layers for high-performance polymer electrolyte membrane fuel cells. ACS Appl. Mater. Interfaces 13, 37004-37013. https://doi.org/10. 1021/acsami.1c06711.
- 59. Gasteiger, H.A., Kocha, S.S., Sompalli, B., and Wagner, F.T. (2005). Activity benchmarks and requirements for Pt, Pt-alloy, and non-Pt oxygen reduction catalysts for PEMFCs. Appl. Catal. B Environ. 56, 9–35. https://doi.org/10.1016/j.apcatb.2004.06.021.
- 60. Borup, R.L., and Weber, A.Z. (2021). M2FCT: million mile fuel cell truck consortium. https:// www.hydrogen.energy.gov/pdfs/review21/ fc339_weber_2021_o.pdf.

- 61. Colón-Mercado, H.R., Kim, H., and Popov, B.N. (2004). Durability study of Pt₃Ni₁ catalysts as cathode in PEM fuel cells. Electrochem. Commun. 6, 795-799. https://doi.org/10.1016/ j.elecom.2004.05.028.
- 62. Wei, Z., Guo, H., and Tang, Z. (1996). Heat treatment of carbon-based powders carrying platinum alloy catalysts for oxygen reduction: influence on corrosion resistance and particle size. J. Power Sources 62, 233-236. https://doi. org/10.1016/S0378-7753(96)02425-1.
- 63. Yu, P., Pemberton, M., and Plasse, P. (2005). PtCo/C cathode catalyst for improved durability in PEMFCs. J. Power Sources 144, 11-20. https://doi.org/10.1016/j.jpowsour. 2004.11.067.
- 64. Xu, F., Wang, M.-x., Sun, L., Liu, Q., Sun, H.-f., Stach, E.A., and Xie, J. (2013). Enhanced Pt/C catalyst stability using p-benzensulfonic acid functionalized carbon blacks as catalyst supports. Electrochim. Acta 94, 172–181. https://doi.org/10.1016/j.electacta.2013.
- 65. Xin, L., Yang, F., Xie, J., Yang, Z., Kariuki, N.N., Myers, D.J., Peng, J.-K., Wang, X., Ahluwalia, R.K., Yu, K., et al. (2017). Enhanced MEA performance for PEMFCs under low relative humidity and low oxygen content conditions via catalyst functionalization. J. Electrochem. Soc. 164, F674-F684. https://doi.org/10.1149/
- 66. Ito, T., Matsuwaki, U., Otsuka, Y., Hatta, M., Hayakawa, K., Matsutani, K., Tada, T., and Jinnai, H. (2011). Three-dimensional spatial distributions of Pt catalyst nanoparticles on carbon substrates in polymer electrolyte fuel cells. Electrochemistry 79, 374-376. https://doi. ora/10.5796/electrochemistry.79.374.
- 67. Zhang, J., Paine, L., Nayar, A., and Makharia, R. (2011). Methods and Processes to Recover Voltage Loss of PEM Fuel Cell Stack. U.S. Patent 0195324 A1.
- 68. Kresse, G., and Furthmüller, J. (1996). Efficiency of ab-initio total energy calculations for metals and semiconductors using a plane-wave basis set. Comput. Mater. Sci. 6, 15-50. https://doi. org/10.1016/0927-0256(96)00008-0.
- 69. Kresse, G., and Furthmüller, J. (1996). Efficient iterative schemes for ab initio total-energy calculations using a plane-wave basis set. Phys. Rev. B Condens. Matter 54, 11169-11186. https://doi.org/10.1103/PhysRevB.54.11169.
- 70. Kresse, G., and Joubert, D. (1999). From ultrasoft pseudopotentials to the projector augmented-wave method. Phys. Rev. B 59, 1758-1775. https://doi.org/10.1103/PhysRevB.
- 71. Perdew, J.P., Burke, K., and Ernzerhof, M. (1996). Generalized gradient approximation made simple. Phys. Rev. Lett. 77, 3865–3868. https://doi.org/10.1103/PhysRevLett.77.3865.
- 72. Greeley, J., and Nørskov, J. (2007). Electrochemical dissolution of surface alloys in acids: thermodynamic trends from firstprinciples calculations. Electrochim. Acta 52, 5829-5836. https://doi.org/10.1016/j. electacta.2007.02.082.